

Exoplanet characterization with nulling interferometry

MSc Thesis

AE5822: MSc Thesis - Space

Lian Greijn

Exoplanet characterization with nulling interferometry

MSc Thesis

by

Lian Greijn

Student Name	Student Number
Lian Greijn	4832787

Supervisors: J.J.D. Loicq and R. Laugier
Project Duration: March, 2024 - March, 2025
Faculty: Faculty of Aerospace Engineering, Delft

Cover: Southern Ring Nebula (NIRCam Image) JWST, by NASA, ESA, CSA, STScI.

Style: TU Delft Report Style, with modifications by Daan Zwaneveld

Acknowledgments

With the submission of this MSc thesis my time as a student will be coming to a close. I have had an incredible time during the past six years in Delft during which I have grown so much, both personally and academically. While I treasure mostly happy memories there were certainly some hardships along the way. I could not have completed my degree, and in its culmination, this thesis without the support of many people.

First of all, I would like to thank my daily supervisors in this project. I first became interested in nulling interferometry during a (very inspiring) lecture by Jérôme Loicq in the course on optical space instrumentation. After his lecture was quickly determined to learn more about the topic. Jérôme connected me early on with Romain Laugier at KU Leuven and so the project was born. I want to thank both of them for their support over the course of this thesis. I felt that I could ask any questions I had and they always provided me with useful and constructive feedback. I also want to thank Ida Sigusch for our frequent conversations together that greatly helped me with ordering my thoughts and my confidence in my own work.

Writing a thesis can sometimes be quite daunting and it becomes a lot easier when sharing your struggles with your peers. I therefore especially want to thank everyone I worked with together, first in 2.56 and later in 6.19. This process would never have been as smooth if not for our energizing coffee breaks and our daily campus walks. I also want to thank all my other friends that supported me during my time at university, especially my fellow board members at the VSV. Finally, I would like to thank my parents and my brother for all their support and love from home.

*Lian Greijn
Delft, March 2025*

List of Figures

Figure number	Figure description
<i>Part I</i>	<i>Literature</i>
Figure 2.1	Young's double slit experiment setup.
Figure 2.2	Comparison of monochromatic and polychromatic fringes
Figure 2.3	contrast of a simulated solar system at 10 pc
Figure 2.4	Schematic overview of a two telescope Bracewell nulling interferometer
Figure 2.5	Component block diagram of a Bracewell nulling interferometer
Figure 2.6	Differential transmission map for a rectangular four telescope nulling interferometer
Figure 2.7	Modulation signal at a range of spectral bins between 4-18 μm for a rectangular four telescope nulling interferometer
Figure 4.1	Graphic representation of the matrix model introduced by Guyon
Figure 4.2	Sketch of the relative array positions of the compared architectures
Figure 4.3	CMP of the operations described by the combination matrix for the double Bracewell nuller
Figure 4.4	Transmission maps of the raw outputs for the linear double Bracewell
Figure 4.5	Transmission maps of the raw outputs for the rectangular double Bracewell
Figure 4.6	Differential transmission map of the linear double Bracewell configuration
Figure 4.7	Differential transmission map of the rectangular double Bracewell configuration grey bars in the plots
Figure 4.8	Modulations of the linear and rectangular double Bracewell configurations
Figure 4.9	The distribution of the nuller outputs after a single nulling step during the observation of a binary object with a modeled 50 nm RMS residual piston excursion
Figure 4.11	CMP of the operations described by the combination matrix for first stage of the kernel nuller
Figure 4.12	CMP of the operations described by the full combination matrix of the kernel nuller
Figure 4.13	Transmission maps of the six dark outputs of the 4 telescope Kernel configuration at wavelength bin 4 μm
Figure 4.14	Differential transmission maps of the kernel configuration
Figure 4.15	Modulation signals for at all spectral bins for the kernel setup
Figure 5.1	Block diagram showing the main steps of SCIFYsim used in this research
Figure 5.2	Example of the retrieval process of the model at $\lambda = 12 \mu\text{m}$
Figure 5.3	Block diagram of the fitting process in SCIFYsim from the input of the planetary parameters to the retrieval of the modulation
<i>Part II</i>	<i>Scientific Paper</i>
Fig. 1	Geometrical layout of the apertures
Fig. 2	Differential transmission map for an on sky view of 600 by 600 mas of the linear double Bracewell architecture
Fig 3	Differential transmission map for an on sky view of 600 by 600 mas of the rectangular double Bracewell architecture
Fig. 4	Differential transmission maps for an on sky view of 600 by 600 mas of the kernel nuller at spectral bin $\lambda = 4 \mu\text{m}$
Fig. 5	The modulation signals in a noise-free case for the three configurations following from the transmission maps at spectral bin 6.4 μm
Fig. 6	Modulation efficiency of the rectangular array at $\lambda = 18 \mu\text{m}$ and at $\lambda = 4 \mu\text{m}$

Figure number	Figure description
Fig. 7	Modulation efficiencies as a function of separation for each spectral channel
Fig. 8	Sketch of the observed planetary system viewed face-on
Fig. 9	Sketch showing the setup of a corner plot
Fig. 10	Sketch of the correlation mapping approach
Fig. 11	Sketch of the modeled two planet system
Fig. 12	MCMC-fitting results from the single planet modeled system with respect to a varying planet radius
Fig. 13	Corner plot of MCMC fitting in a single planet case
Fig. 14	Correlations between the parameters as function of the planet position for the three compared configurations
Fig. 15	Standard errors associated with the parameter fitting as a function of the planet position
Fig. 16	Matched filter maps for the three configurations for a two planet case
Fig. 17	Fitting results of the two planet fitting
<i>Part III</i>	<i>Appendix</i>
Figure A.1	Transmission maps resulting from the beam combination in the linear double Bracewell nuller
Figure A.2	Differential transmission map of the linear double Bracewell configuration at respectively $4 \mu\text{m}$ and $18 \mu\text{m}$
Figure A.4	Signal modulations for the linear configuration, for a planet located at $[0, 100]$ in case of no noise
Figure A.5	Transmission maps resulting from the beam combination in the rectangular double Bracewell nuller
Figure A.6	Differential transmission map of the rectangular double Bracewell configuration at respectively $4 \mu\text{m}$ and $18 \mu\text{m}$
Figure A.7	Signal modulations for the rectangular configuration
Figure A.8	Modulation efficiencies for the rectangular configuration
Figure A.10	Differential transmission maps for the kernel configuration showing the recombination of the six dark outputs
Figure A.11	Signal modulations across the spectral regime for the kernel configuration
Figure A.12	Modulation efficiencies for the rectangular configuration
Figure A.13	MCMC corner plot result in a larger format
Figure A.14	MCMC fitting results with a varying planet separation
Figure A.15	Single fitting results for a single planet with a varying planet temperature
Figure A.16	Single planet fitting w.r.t. radius without zoom
Figure A.17	Maps of the correlation levels between each parameter pair with indication of $\lambda/2B$
Figure A.18	Results of a two planet fitting with two planets

List of Tables

Table number	Table description
Table 3.1	Global planning for the identified thesis tasks including the expected duration.
Table 5.1	A selection of functions within SCIFYsim to interact with the simulation object
Table 5.2	Planetary parameters used in the model
Part II	<i>Scientific Paper</i>
Table 1	Mission parameters used in the configuration of the simulator for the single spacecraft testbed
Table 2	Observation parameters used in the SCIFYsim simulations

Contents

Acknowledgments	i
List of Figures	ii
List of Tables	iv
Nomenclature	vii
1 Introduction	1
1 Literature	2
2 Foundations of nulling interferometry	3
2.1 Interferometry for space observations	3
2.2 Nulling interferometry for exoplanet detections	5
2.3 Concept legacy	6
2.3.1 Darwin and TPF	6
2.3.2 Pegase	6
2.3.3 The Palomar Fiber Nuller (PFN)	7
2.3.4 NOTT	7
2.3.5 LIFE	7
2.4 Architecture of a space-based nulling interferometer	7
2.5 A nulling interferometer's signal	7
2.6 External noise sources	10
2.6.1 Host star	10
2.6.2 Local Zodiacal Dust	10
2.6.3 Exozodiacal Dust	11
2.7 Internal noise sources	11
2.7.1 Thermal background noise	11
2.7.2 Detector noise	11
2.7.3 Instrumental errors	11
3 Research setup	13
3.1 Research question	13
3.2 Thesis planning and tasks	14
3.2.1 Reflection on original planning	14
4 Nulling interferometer configurations	16
4.1 Single Bracewell versus double Bracewell	16
4.2 Guyon's Matrix model	16
4.3 The compared configurations	17
4.3.1 The double Bracewell nullers	18
4.3.2 The Kernel configuration	21
5 SCIFYsim	25
5.1 Initializing a simulation in SCIFYsim	25
5.2 Modifications to SCIFYsim	26
5.3 Generating the noisy signals	26
5.4 Retrieving planetary parameters	27
5.5 Origin and impact of correlations	28

II Scientific Paper	29
III Appendices	43
References	44
A Additional Figures	46
A.1 Configuration specific figures	46
A.1.1 Linear double Bracewell configuration	46
A.1.2 Rectangular double Bracewell configuration	46
A.1.3 Kernel four telescope configuration	50
A.2 Additional results	52
A.2.1 Single planet	52
A.2.2 Correlations	53
A.2.3 Two planets	53

Nomenclature

Abbreviations

Abbreviation	Definition
CNES	Centre national d'études spatiales (French space agency)
COBE	Cosmic Background Explorer
ESA	European Space Agency
FoV	Field of View
HOSTS	Hunt for Observable Signatures of Terrestrial planetary Systems
LIFE	Large Interferometer for Exoplanets
LMFIT	Non-Linear Least-Squares Minimization and Curve-FITting for Python
MC	Monte Carlo
MCMC	Markov Chain Monte Carlo
NASA	National Aeronautics and Space Agency
NIR	Near Infrared
MIR	Mid-infrared
ODL	Optical Delay Lines
OPD	Optical Path Differences
PFN	Palomar Fiber Nuller
QE	Quantum Efficiency
SCIFYsim	Self-Calibrated Interferometry For exoplanet spectroscopy
SNR	Signal to Noise Ratio
TPF-C	Terrestrial Planet Finder Coronagraph
TPF-I	Terrestrial Planet Finder Interferometer
VLT	Very Large Telescope Interferometers

Symbols

Symbol	Definition	Unit
B	Baseline	[m]
B_λ	Spectral radiance	$[\frac{W}{sr \cdot m^3}]$
c	Speed of light	[m/s]
F	Flux	$[ph/m^2]$
I	Intensity	$[ph/m^2]$
PA	Position angle	[deg]
R	Planet Radius	$[R_e]$
Sep	Planetary separation	[mas]
T	Temperature	[K]
λ	Wavelength	[m]
θ	Angular Resolution	[arcsec]
Ω	Solid angle	[sr]

1

Introduction

Since the first detection of an exoplanet in 1992 [38], the number of confirmed exoplanets has exploded, with thousands of new detection over the last decades. Currently employed detection methods, such as transit spectroscopy, radial velocity and gravitational micro-lensing, allow the determination of some global planetary parameters. However, with all these new discoveries the focus of new research is shifting towards a more detailed characterizations of these worlds, also highlighted in the Voyage 2050 vision of the European Space Agency (ESA):

...being able to detect infrared light directly emitted by those atmospheres will be key in understanding the chemical and physical diversity of these temperate worlds and whether they harbour truly habitable surface conditions. [36]

To achieve the direct detection of photons from these distant planets a variety of challenges need to be overcome. The most critical of these are (1) blocking the stellar light in order to reveal the much fainter planet and (2) the high angular resolution required to resolve the planet from the close-by star. A possible strategy to overcome these issues, especially in the desired mid-infrared wavelength, is the use of space-based nulling interferometry. In the nulling interferometer the incoming light is combined in such a way that the stellar light is interfered destructively, or nulled, and the planetary companion is preserved in a constructive combination.

In the early 2000's, two proposals were created to develop a formation flying, nulling interferometry mission. However, neither of these concepts came to fruition, mostly due to technological and budgetary constraints [26, 3]. Now, almost two decades later, many technological strides have been made and a new mission initiative is being developed, the Large Interferometer for Exoplanets (LIFE) [31]. This revival of interest for a space-based nulling interferometry mission is paired with the need to prove the required technology. While ground based initiatives have successfully developed nulling interferometers, it has not yet been demonstrated in a space environment.

In order to test the technology in a space environment, a simpler precursor mission is recommended. Current focus is placed on a smaller, single spacecraft [27]. For this mission three possible designs are being considered, a rectangular double Bracewell, a linear double Bracewell, and a diamond-like kernel nuller design. In this research these designs will be compared based on their ability to constrain four planetary parameters, the planet's temperature, radius, separation and position angle.

This thesis report is divided into three parts. Part I provides an introduction to the topics treated in this work; in chapter 2 the principles of nulling interferometry are introduced, following this in chapter 3 the setup of the research and the research question are introduced. From this some additional background on the compared configurations and the model setup are provided in respectively chapter 4 and chapter 5. Secondly, in Part II, the work performed in this research is presented in the format of a scientific paper. Finally Part III, provides the appendices to this work, including the bibliography and a selection of additional figures in Appendix A.

Part I

Literature

2

Foundations of nulling interferometry

Before the first exoplanet was officially detected, Bracewell, in 1978, made the proposal to use nulling interferometry for the direct observation of exoplanets [5]. This chapter will discuss the foundations of this principle and serve as a more in-depth explanation for readers unfamiliar with the topic. The chapter will begin an introduction to nulling interferometry and will discuss some of the previous and current projects and proposals employing the technique. Following this, the architecture of a nulling interferometer will be discussed and finally a look will be taken at the signal that is obtained from the instrument.

2.1. Interferometry for space observations

The angular resolution of any optical instrument is fundamentally limited by the diffraction of light in the system, known as the *diffraction limit*. The angular resolution dictates the minimum resolvable feature size in an image and is dependent on the aperture size and wavelength. For a conventional telescope with a circular aperture, the fundamental angular resolution can be calculated using Equation 2.1 [17], where θ is the angular resolution in radians, λ is the observed wavelength in meters and D is the aperture diameter in meters.

$$\theta = 1.22 \frac{\lambda}{D} \quad (2.1)$$

Pushing the angular resolution of a system observing at a given wavelength thus requires an increase in its size. To resolve a planet located with the same separation of Earth from a star at $10 \mu\text{m}$, located a distance of 10 parsec, would require a diameter of at least:

$$\begin{aligned} \theta_{\text{earth-sun}} &= 100\text{mas} \\ D &= \frac{1.22 * 10e^{-6}\text{m}}{100\text{mas}} \approx 25\text{m} \end{aligned}$$

Roughly four times bigger than the James Webb Space Telescope. To avoid having to build such large, complex, and therefore very expensive, instruments the principle of interferometry can be employed. Interferometry with visible light was first demonstrated in the double-slit experiment by Thomas Young, he showed that combining light from a coherent source propagated through a double slit creates an interferometric fringe pattern. A visual representation of his setup is provided in Figure 2.1.

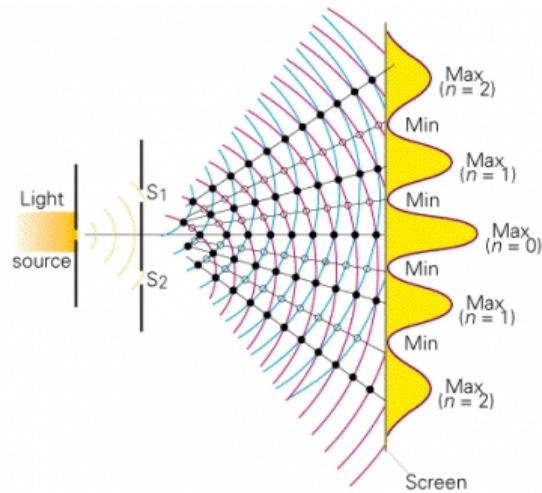


Figure 2.1: The double slit experiment setup used by Young. Light propagates through 2 closely placed slits s_1 and s_2 , diffraction occurs and the superimposed wavefronts create an interference pattern at the screen [4].

The spacing of the fringes recorded on the screen is a function of the distance between the two slits, in Figure 2.1 denoted by s_1 and s_2 through the relation in Equation 2.2. Where x is the spacing between the maxima in meters, F is the focal distance to the screen and b denotes the baseline, defined as the distance between the slits. Transferring this concept from slits to multiple telescopes, it is no longer the individual aperture diameter in Equation 2.1 that dictates the angular resolution, but the baseline between the apertures.

$$\Delta x = \frac{\lambda F}{b} \quad (2.2)$$

However, combining light from multiple telescope in such a way that the desired fringe pattern is created is not a trivial problem, and some important caveats should be taken into account.

About 150 years before Thomas Young, a very similar experiment to his was attempted by Grimaldi. He tried to study the interaction between two light beams by letting sunlight enter through two small pinholes and capturing the results on a screen. His experiment, however, failed. The critical improvement to the setup of the experiment by Young was to let the incoming light pass through a pinhole before reaching the slits, therefore greatly reducing the size of the light source [17].

In order to have obtain an interference pattern, it is important that the light is coherent. This coherence has two aspects: temporal coherence and spatial coherence [17]. Temporal coherence means that the phase of the light is constant over a certain period of time and it is influenced by the bandwidth of the source. Spatial coherence is defined by a constant phase of the light at different points in space; for example, across the wavefront itself it is influenced by the physical extension of the source, and thus what made Grimaldi's experiment fail.

Incoherent sources, such as stars, can still end up producing coherent wave fronts as long as there is a large distance between the source and the observation of the wavefront [34]. To create a useful interference pattern it is essential that the wavefront is coherent.

The second potential issue with creating a clear interference pattern is related to the wavelength dependence of the fringe spacing, described in Equation 2.2. Due to the polychromatic nature of a stellar source, the fringe pattern it creates has a different fringe spacing at each wavelength for the given baseline. This will cause the fringes to start blurring together causing a decrease in the contrast. The effect can be observed in Figure 2.2.

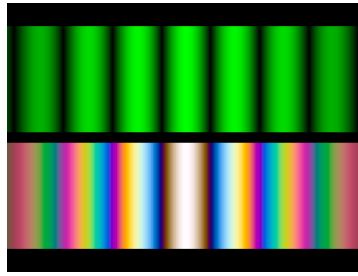


Figure 2.2: Comparison of the fringe pattern for monochromatic light on top and white (polychromatic) light at the bottom. It can be observed that in the polychromatic case the wavelength dependency of the interference location causes a blurry spread of the different colors making up the light.

1

2.2. Nulling interferometry for exoplanet detections

Now that the basic requirements for achieving stable interference have been discussed, a closer look can be taken at how it can be employed to an exoplanet detection mission. In order to detect exoplanets the two critical challenges are the high angular resolution needed, as was shown in section 2.1, and secondly the extreme contrast between a very bright star and a faint planet. For the Earth and Sun in visible light this is in the order of 10^9 , as shown in Figure 2.3. However, if the planet is instead observed in the mid infrared around $10 \mu\text{m}$, this difference in brightness reduces to about 10^6 .

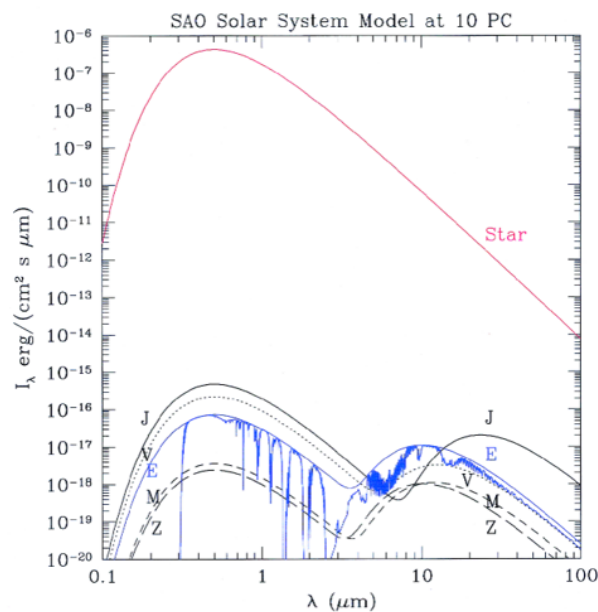


Figure 2.3: The model spectrum of the sun and the solar system planets for an observer at 10 pc. The difference between the Earth spectrum and the peak of the stellar spectrum is about 9 orders of magnitude [11]

In the most simple setup the nulling interferometer, as described by Bracewell in 1978 [5], uses two apertures, leading to the transmission pattern shown in Figure 2.2. To null the stellar light a destructive section of the created pattern should be placed over the on-axis star, requiring a π phase shift to be applied to one of the beams. The goal is then to catch the off-axis planet in constructive segment of the created pattern. This setup is visualized in Figure 2.4.

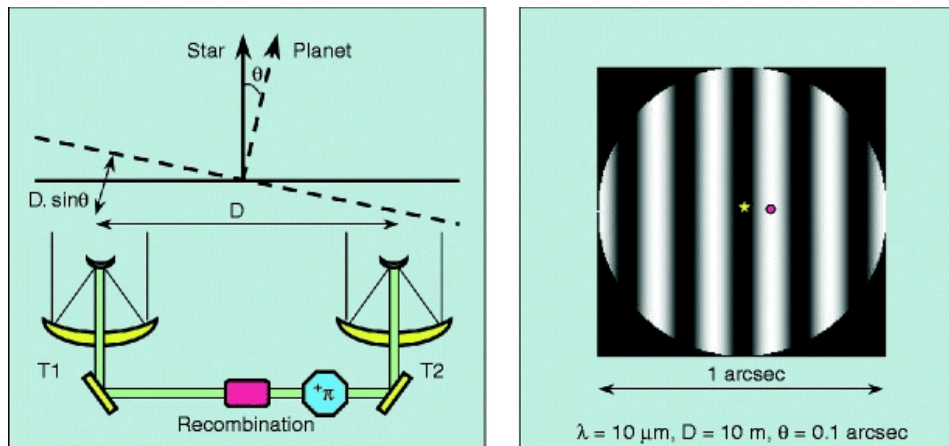


Figure 2.4: Schematic overview of a Bracewell nulling interferometer, where the light of the target star and off-axis companion is gathered by 2 apertures, labeled T1 and T2, spaced by a baseline D . The beams are recombined after a π phase shift is applied to the light recorded in T2. On the right the resulting fringe pattern is drawn displaying the star in the null-fringe and the planet in a constructive one [33]

2.3. Concept legacy

In the decades since the original proposal the concept has been developed considerably. The developments in the field have yielded more advanced designs and have identified issues that might occur when using the relatively simple design shown in section 2.2. In ground based observatories successful nulling interferometers have been implemented. There have been several proposed space based missions to employ nulling interferometry for the detection of exoplanets, however none have actually been build so far. Below follows a brief overview of the previous proposals to provide more context on where current developments stand.

2.3.1. Darwin and TPF

In the early 2000s two mission proposals were submitted both proposing the use of a nulling interferometer for terrestrial exoplanet detection. Darwin [26], submitted to ESA, and TPF, Terrestrial Planet Finder, to NASA. Both ended up not being selected predominantly due to technological challenges and budget issues [32].

Darwin proposed a four aperture design called the Emma-type X-array. This layout uses four spacecraft in a rectangular plane with a baseline ratio of 1:3 to collect the incoming light and proceeded to send the beam to an out-of-plane combiner spacecraft located 1200 m above the array [26]. The mission would observe in the mid-infrared, specifically the 6-20 μm wavelength domain.

The TPF proposal was later split into a combination of 2 types of observation techniques: the TPF-C, as single aperture coronagraph and the TPF-I, a multi-aperture nulling interferometer. TPF-I was initially proposed as a 3-4 element array of telescopes to collect the incoming light. The selected observational wavelength was similar to Darwin, between 6-18 μm [3]. Over the course of some design iterations the TPF-I team also eventually selected the Emma X-Array design, like Darwin. The mission specific studies were ceased in 2007 and focus was relayed to identifying and developing required technologies and setting up precursor missions that could help with maturing technology [22].

2.3.2. Pegase

Another proposed nulling interferometer mission was Pegase, initially submitted to the French national space agency CNES and later also to ESA [30]. The idea of the mission was to serve as a pathfinder mission to Darwin/TPF-I. Instead of terrestrial, Earth-like planets its main scientific objective would be to perform spectroscopy measurements of hot Jupiters, also known as Pegasides, and brown dwarfs. It would observe these targets in the Near infrared (NIR) [25]. A two aperture configuration was proposed with aperture diameters of 40 cm and a baseline ranging between 50 and 500 m [24]. Like Darwin an TPF the proposal eventually stranded, however it did lead to a test facility to test the feasibility of a stable polychromatic null [18].

After these three proposals halted development focus was relayed into maturing the technology required for such ambitious missions. More recent developments are described below.

2.3.3. The Palomar Fiber Nuller (PFN)

The PFN is a ground based instrument built in support of future space based missions. The goal of the PFN was principally to demonstrate the possibility of detecting a stellar companion by artificial rotation of the baseline. Interferometers on Earth mostly rely on the rotation of Earth, which is of course not feasible for a space-based system. Additional important goals were to prove that detection was possible at much smaller angles than would be possible using coronagraphy, to reach deep nulls of order 10^{-4} , and finally to expand the nulling techniques from the MIR to the NIR region, where phase instability becomes a dominant source of noise [35].

2.3.4. NOTT

NOTT is currently being developed as the first nulling interferometer instrument at the Very Large Telescope Interferometer (VLTI) [9]. The main goal of NOTT would be to observe young giant exoplanets which are located very closely to the star [21]. The instrument would operate at a much smaller wavelength range between 3.5-4 μm and combine the light of the four telescopes at the VLTI site.

2.3.5. LIFE

The Large Interferometer for Exoplanets (LIFE) project is an ongoing initiative for a new large space nulling interferometry mission proposal, building on the legacy left by Darwin and TPF-I. The goal of LIFE is to detect and characterize Earth-like exoplanets [31].

The current design proposal for LIFE is a double Bracewell formation flying system with four collector spacecraft, similar to the Darwin and TPF-I design proposals. The mission would operate at a spectral range between 4-18.5 μm and the baselines should be able to vary between 10 to 600 m [14]. Due to the maturing of the technology over the last decades, for example related to coordinated formation flying, and a more extensive knowledge of the exoplanet population, it is believed by the initiators that the mission may this time come to fruition. The LIFE initiative also forms the main context for this research.

2.4. Architecture of a space-based nulling interferometer

In Figure 2.4, a simplified schematic of a nulling interferometer was shown. In practice there are a number of components required between the telescopes capturing the light and the subsequent combination. A more detailed overview of a possible optical architecture of a nulling interferometer can be found in Figure 2.5.

Importantly, several corrections need to be applied to the wavefront before a coherent combination is possible. In this design the first correction to the incoming wavefront is performed by the tip/tilt-mirrors, which correct the corresponding tip/tilt errors. Following this, the system contains Optical Delay Lines (ODL), which correct Optical Path Differences (OPD). These OPDs can originate from orientation of the platform with respect to the target, but also within the system due to imperfections in the optical design. The level of correction required is determined by the respective sensors. The beam is then injected into an optical fiber and an achromatic phase shift is applied to one of the beams.

This particular design proposes the use of optical fibers, but other optical components, such as bulk optics or integrated optics can be used. This thesis will predominantly investigate the signal of a nulling interferometer and the hardware in the instrument will be modeled in a simplified way, more details on the modeling approach will follow in chapter 5. It is important to note, that the hardware development is still an ongoing process and the selected hardware components will also impact the quality of the signal.

2.5. A nulling interferometer's signal

After the light has traveled through the optical train and has been successfully combined, the result is recorded on the detector. Unlike a traditional telescope it is not an image of the scene that is recorded. The detector of the system records the flux after combination in preselected wavelength bins. It is not

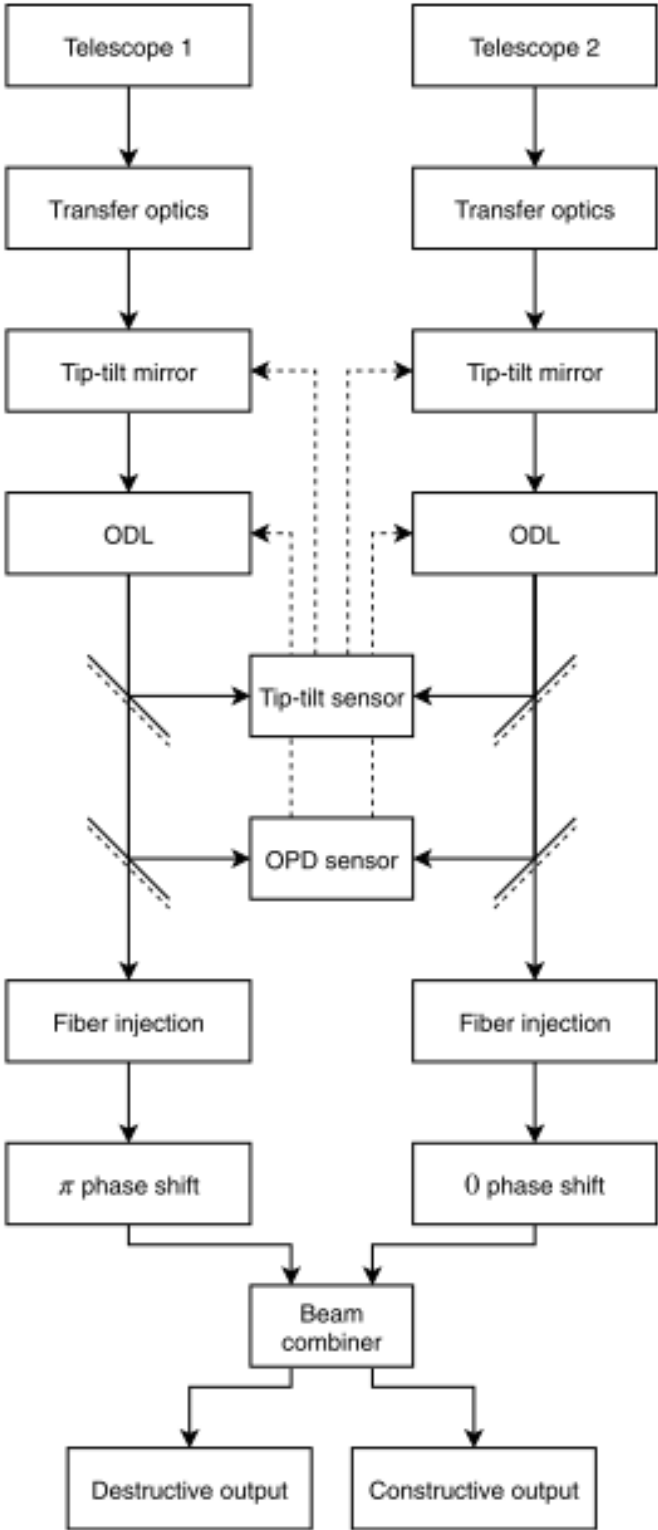


Figure 2.5: Block diagram of a Bracewell nulling interferometer optical train. The light enters from the top of the diagram and follows the solid arrows through the system. The dotted lines represent feedback loops which control the wavefront correction components. [6]

a single exposure moment that provides the information, but the temporal modulation of the signal as a result of the rotation of the spacecraft. This modulated signal is then fitted to a model system in order to retrieve information from the observed scene.

It is therefore important to model the signal as it travels through the instrument and make an accurate prediction of the signature of a model planetary system to fit the results. For this research a preexisting nulling interferometry simulator Self-Calibrated Interferometry For exoplanet spectroscopy simulator (SCIFYsim) was used, which was originally developed for NOTT, see subsection 2.3.4. More details on this simulator can be found in chapter 5

To visualize what the nulled signal will look like, a transmission map can be used. The transmission map can be seen as a sieve of the instrument response. It visualizes the transmission pattern over the Field of View (FOV), showing which segments of the scene are 'nulled' and which are constructively interfered as follows from the positions of the architecture. The transmission map therefore shows where the flux on our detector originates from, an example was shown in Figure 2.4.

The transmission map is the result of the telescope configuration, the observational wavelength, and the FOV of the instrument. Therefore, it is not a single static map. It will rotate, due to the spacecraft rotation, and scale, as a function of wavelength; the extent of the pattern will be determined by the FOV.

A four telescope rectangular setup, with two destructive outputs, leads to the differential transmission maps shown in Figure 2.6. The use of differential meaning that the two dark outputs are subtracted from each other, creating a single map and also leading to negative values in the plot, more information on this process will be provided in chapter 4. The scaling effect between the two wavelength bins, 4 and 18 μm , shown is clearly significant.

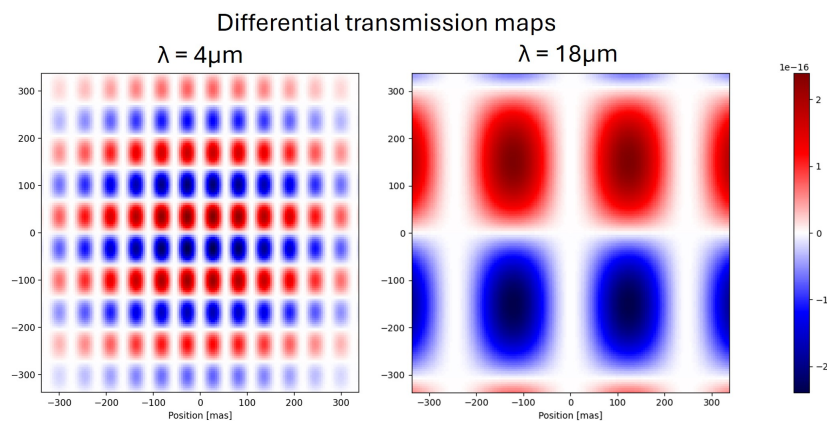


Figure 2.6: Differential transmission map for a rectangular four telescope nulling interferometer with telescope diameter of 3 m and a baseline of 15 m at wavelengths of respectively 4 and 18 μm . The coloring indicates the number of photons/s/m²

For the provided transmission maps it is now possible to plot the hypothetical 'perfect' signal for this particular architecture. If a planet were located at the point (0, 100) in the map and the modulation of the signal intensity due to the rotation of the spacecraft was recorded at a range of spectral bins between 4-18 μm , the modulated signal would look like Figure 2.7. It is this signal that is recorded at the detector and which is used in order to fit a model to the observations.

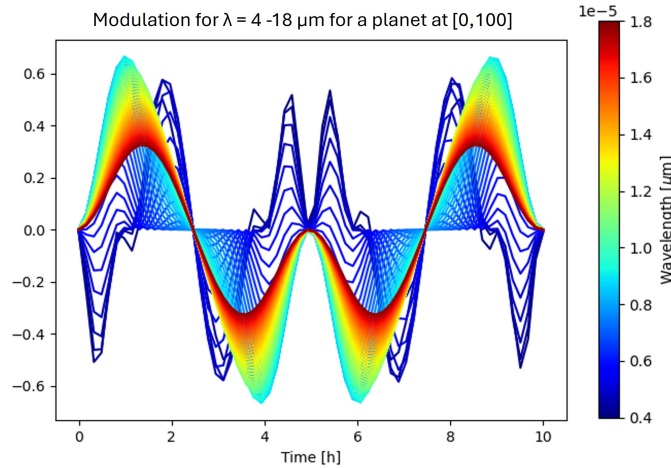


Figure 2.7: Modulation signal at a range of spectral bins between 4-18 μm for a rectangular four telescope nulling interferometer during an observation period of 10 hours.

2.6. External noise sources

In practice a lot of noise is present in the signal received in the detector. This noise has a variety of origins, both within the instrument and due to external factors. This section will briefly discuss the noise sources affecting the signal and discuss possible mitigation strategies.

2.6.1. Host star

The first, and most obvious source of noise, is the host star itself. The star's signal can leak through the nulling pattern in two ways. Firstly, in relation to the null depth, which is defined as the level of suppression in the null, or mathematically described in Equation 2.3. Where I_+ is the intensity at the constructive output and I_- at the destructive output [7]. Even in the ideal case, having the star exactly centralized on the strongest, central null some of the stellar light will not be fully suppressed, decreasing the depth of the null and thereby leaking through into the signal[6].

$$N = \frac{I_-}{I_+} \quad (2.3)$$

Similarly, due to the extended nature of the star, it is also possible for stellar light to leak due to an insufficient width of the null. This leads to a potential issue in the design, where the desire to cover the full star potentially also blocks light from close-by planets. Even with very deep and wide nulls some stellar leakage is to be expected in the final signal.

2.6.2. Local Zodiacal Dust

The solar system contains a large amount of dust. Problematic for detecting exoplanets is especially the zodiacal dust. Zodiacal dust is hypothesized to be the result of collisions of planetesimals in an outer ring which migrate inwards and the result of comets disintegrating when they reach the inner parts of the planetary system [12]. In the solar system it is situated between the orbits of Mercury and Jupiter and it scatters light from the sun. The dust can even be seen with the naked eye [13]. It scatters light predominantly in the mid-IR, which is the desired observational wavelength for a terrestrial planet finding mission, thereby possibly hindering observations.

During NASA's COBE (Cosmic Background Explorer) mission, which measured and mapped the cosmic microwave background, it was critical to remove any foreground effects caused by the interplanetary dust. This led to a detailed measurement and developed model of the local zodiacal dust [19] and its effects can be partly mitigated. The dust has a peak in the ecliptic, therefore for observation it is beneficial to observe away from the ecliptic to minimize the impact on the signal.

2.6.3. Exozodiacal Dust

Analogue to our own solar system, the orbital plane of exoplanet systems also contains so-called exozodiacal dust. Similar to the local zodiacal dust, it is brightest when observing in the mid-IR, leading to photon noise in observations. The symmetric effects are eliminated due to the array rotation, however asymmetric structures in the clouds can pose problems [10].

A recent survey, Hunt for Observable Signatures of Terrestrial planetary Systems (HOSTS, [12]), aimed to characterize the exozodiacal dust in nearby systems. The survey found that systems with cold debris disks are likely to also have prohibitive, high levels of dust in the habitable zone and are typically not great targets for finding exo-Earths. To mitigate the impact of the dust on a mission it is recommended to only observe systems that have relatively low levels of exozodiacal dust. The effect of the dust will be larger at longer wavelengths and for more distant, fainter targets [12]. Issues are also expected with spectroscopy, during which the dust will most likely become more of a nuisance due to long integration times [12].

2.7. Internal noise sources

The external noise sources discussed above are assumed to be the dominant noise sources. However, the optical system and spacecraft itself can also introduce noise and potential errors which can significantly impact the quality of the measurements. This section will briefly discuss the noise sources originating from the system itself.

2.7.1. Thermal background noise

Firstly, the spacecraft itself is illuminated by the sun and as a result it heats up. It will therefore also radiate some thermal flux that will leak into the signal. To account for this during the design, the system can be modeled as a gray body as was done in previous work [6].

2.7.2. Detector noise

Secondly, the detectors used in any system are not perfect. Not every photon that enters the system is detected properly by the detector. The measure of the detectors ability to transfer the photons to an electron signal is expressed by the Quantum Efficiency (QE) in the detector. The response of the detectors is not always uniform over the bandwidth. In previous work an estimate of a QE at about 80% was used [6].

2.7.3. Instrumental errors

The final, and currently least quantified internal source of errors, are the expected instrument perturbations and errors originating from the optical train itself.

Due to the tight phase tolerances to perform coherent optical interference slight perturbations in the system can create unexpected signals. In Figure 2.8 a simulated signal is presented. If the system is pointing even slightly off axis from the target, it can be extremely hard to identify whether the resulting signal is due to the presence of a planet or due to off-axis stellar light.

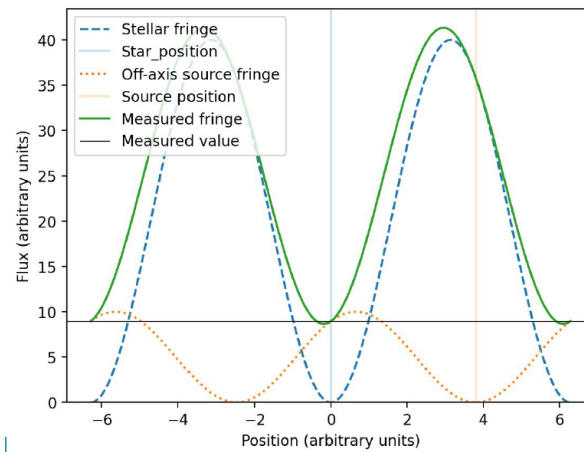


Figure 2.8: Simplified response of a nulling interferometer showing the signal contributions as a result of an off-axis source (orange) and a host star (blue). A perturbation of the null means that the minimum of the green line is no longer centered. The measured signal of the star could then drown the planet signal.

Sources of instrumental errors can include imperfections in the instrument amplitude or phase response as the light beam moves through the optical system, polarization effects, and fluctuations in stray light reaching the system. A detailed discussion and mathematical derivation of these error sources by Lay can be found in [23]. To perform successful nulling interferometry there are important requirements on the stability of the null. The quantification of the instrumental errors that may occur in the instrument is still an ongoing topic of research.

3

Research setup

Following this initial look into the general principles of nulling interferometry, this chapter will provide information on the setup of the research itself. First in section 3.1, the research question that forms the focus of this document will be introduced. Following this the created planning including a short reflection can be found in section 3.2.

3.1. Research question

In section 2.3, a short overview was provided of previously developed mission proposals and ground based instruments. The research supporting these initiatives has lead to a variety of new nulling techniques and have also identified new challenges that may occur over the course of the mission. Importantly, before a large scale mission could take place it is recommended that the technology is first proven in a smaller precursor mission. In support of the current LIFE initiative a variety of simulations and estimations of the systems performance have been completed, [32, 8, 16]. These simulations have mostly neglected the presence of instrumental noise and assume large designs with reconfigurable baselines.

The question thus arises if these results also translate to a smaller mission; what would be the optimal design when reconfiguration of the baselines is not an option and the baselines are much shorter. Additionally, what if the instrumental effects are not neglected in the simulations and how will this impact the quality of the results that can be obtained? Combining these topics the research question that is aimed to be answered in this thesis is:

How does a 4-telescope kernel nuller compare to a double Bracewell configuration when providing constraints on top-level planetary parameters during a fixed baseline space-based nulling interferometry mission aimed at detecting and characterizing terrestrial exoplanets

In this research two common variations of the double Bracewell nuller will be compared, a rectangular setup and a linear setup. Each of the compared configurations will have four collecting telescopes and a maximum length of 15 meters. The top level planetary parameters in the question refers to the retrieval of the planet's temperature, radius and position with respect to the star.

From this research question a number of global steps were identified towards the end of the literature phase that need to be completed. These were determined to be:

1. Finding the comparison metric, what are the configurations assessed on?
2. Creating comparative models for the architectures. Which software can used for the modeling of the systems? Which assumptions and simplifications are used?
3. Set up of the test cases in the model. E.g. the type of planetary systems (single vs. multi planet)? What characteristics govern these systems? What starting parameters are used in the model?
4. Executing the comparison itself and displaying of the results.

5. Performing an analysis of the statistical significance of the results. E.g. what are the associated confidence intervals? How certain can we be of the results? Performing a sensitivity analysis.
6. Drawing final conclusion and reporting of the results.

Before moving on to the corresponding planning, the first two items were prepared before starting the programming section of the work. Firstly regarding the comparison metric it was chosen to look at the performance in three categories:

1. **Single planet case**, how well are the configurations able to constrain the parameters when a single planet is modeled?
2. **Correlation levels**, how are the parameters correlated in the fitting process?
3. **Two planet case**, how well are the configurations able to retrieve the planetary parameters in a two planet system?

Previous simulations predominantly use the SNR as the performance metric in the comparison. In this study the choice was made to look beyond just this ratio and also try to retrieve the general parameters. It was especially expected that the presence of instrumental noise sources leads to additional correlations in the data. To provide a more complete analysis and also address potential overestimation on the actual performance based on solely the SNR the focus was shifted to the behavior of these four parameters. The ability to constrain the parameters will be assessed based on the proximity of the fitted parameter mean to the 'true' value and the corresponding error bars. To incorporate instrumental effects the software SCIFYsim was chosen, more details on this decision will follow in chapter 5.

3.2. Thesis planning and tasks

After the topic and general approach was prepared it was possible to start identifying individual tasks to be completed. The tasks and the expected duration of them is presented in Table 3.1.

Table 3.1: Global planning for the identified thesis tasks including the expected duration. The [added] tasks were added later in the research process.

Number	Task	Expected duration
0.1	Familiarization with SCIFYsim	2 weeks
0.2	Setup of the space environment	1 week
0.3	Incorporating support for the Kernel configuration	1 week
0.4	Implement the three configurations	1 week
1.1	Setup of the single planet case (strategy)	1 week
1.2	Implement single planet case in code	1 week
1.3	Running the planned cases	2 weeks
1.4	Display of single planet results	1 week
1.5	Implementation of feedback	1 week
2.1	Modifications of code for correlations	1 week
2.2	Running the cases for correlations vs position	2 weeks
3.1	[added] Setup for assessment two planet system (strategy)	2 weeks
3.2	[added] Implementation of two planet systems	1 week
3.3	[added] Running the planned cases	2 weeks
3.4	[added] Display of the two planet results	1 week
3.5	[added] Implementation of two planet feedback	1 week
Additional		
A.1	[added] Migrate code to be employed on Delft Blue	2 weeks
A.2	Preparation of presentations (midterm+ greenlight)	1 week
A.3	Documentation and reporting	6 weeks

3.2.1. Reflection on original planning

Most of the steps identified in Table 3.1 were executed in roughly the allotted time. However, especially the initial familiarization with SCIFYsim took some extra time. Additionally, it became clear that my

personal workstation was not able to handle the required to run the simulations, which lead to some additional delay and eventually a move towards the Delft Blue server to run the tested cases. This in turn shortened the amount of time that was required to run the simulations. The expansion of the model to a two planet system was implemented once it became clear that there was sufficient time to incorporate this topic, however only a limited amount of cases could be analyzed due to time constraints.

4

Nulling interferometer configurations

As introduced in chapter 3, three different proposed architectures are compared in this research, a linear configuration, a rectangular configuration, and finally a kernel nuller in a diamond configuration. This chapter will provide some details on the properties of each of these configuration. Firstly, some background on multi aperture nullers and the Guyon matrix model will be discussed in section 4.1 and section 4.2. Following this the matrix model will be applied to the three presented configurations and their corresponding properties will be discussed in section 4.3.

4.1. Single Bracewell versus double Bracewell

In section 2.5 it was demonstrated how the signal measured at the detector is directly related to the (relative) positions of the apertures. During the investigations for Darwin and TPF-I it became clear that the two aperture system originally proposed by Bracewell will not reach the performance required for a system observing terrestrial exoplanets. The move was made towards more advanced multi aperture nullers. A design with just two aperture has a number of complications, here just a selection will be discussed.

The first stems from the trade-off between the wish for a wide null, for which a (relatively) short baseline is required, and the need to resolve nearby features, which in turn benefits from a long baseline. This lead to the proposal by Angel & Woolf [2] for a four element linear interferometer. The different baselines could combine to both a deeper and and broader null compared to Bracewell, while retaining the ability to resolve closely situated objects. The second issue is the symmetric response of the Bracewell interferometer [23], which causes any detected planet to have an 180° ambiguity in its position. Preferably a geometry is used which leads to an asymmetric transmission map. Finally, it was initially assumed that the rotation of the system would be sufficient to filter noise sources such as the zodiacal clouds [1]. However in later research it became clear that especially slow variations in stray light and thermal emission can pose issues [23].

4.2. Guyon's Matrix model

With a variety of proposed designs of nulling interferometers the need arises to model the designs in such a way that they can be easily compared. A possible method is the matrix-based approach based on the work of Guyon [15]. The matrix model provides insight in how the incoming light beams are manipulated before reaching the outputs.

The input at the entrance of the apertures is modeled using vector V where each element is a complex amplitude arriving in aperture k with [15]

$$V_k = r_k e^{i2\pi(x_k\alpha + y_k\beta)/\lambda}$$

Where (α, β) describes the angular offset of the point source, x_k and y_k describe the coordinates of the aperture in a 2d array, and r_k is the corresponding aperture radius. The operations of the interferometer

are modeled by matrix U and thus the outputs W are simply presented by the relation

$$W = UV$$

Where the detector measures the intensity, and thus $I = |W|^2$. These notations are also represented graphically in Figure 4.1. The matrix U thus describes how the light from inputs k is sent towards the different outputs. For a four beam nuller, which has one bright output and three dark ones, matrix U can be written as [28]:

$$U = \frac{1}{\sqrt{4}} \begin{bmatrix} 1 & 1 & 1 & 1 \\ 1 & 1 & -1 & -1 \\ 1 & -1 & 1 & -1 \\ 1 & -1 & -1 & 1 \end{bmatrix}$$

The top row describes the bright output, all inputs are constructively sent to the first output. The dark outputs are found in the bottom three rows, where it can be seen how the signals are combined in a different way for each output. The matrix describes an ideal case, in reality it is complicated to direct all the bright signal to a single output. This is only possible if the central source is unresolved and located on the optical axis so α and β are 0 [15].

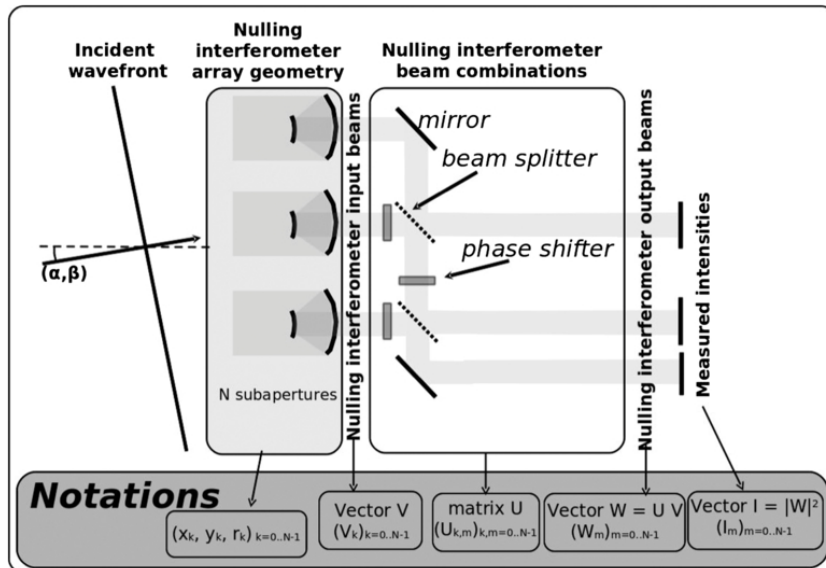


Figure 4.1: Graphic representation of the matrix model introduced by Guyon. The point source is located at angle (α, β) on the left, the incoming wavefront is described by vector V , the operations of the interferometer by matrix U and the final output by matrix W . The final detector measures the intensity describes by $|W|^2$ [15]

4.3. The compared configurations

As introduced in subsection 2.3.5, the research performed in this thesis is in support of the LIFE initiative, specifically in context of a smaller precursor mission proposal, which aims to demonstrate some key technologies. Therefore, the configurations in this research have a relatively short baseline compared to the goals of the LIFE mission. To keep the comparison fair, the configurations all have four circular collecting apertures with a diameter of 2 meters. The maximum baseline is 15 meters and all apertures are located in the same plane.

A sketch of the geometrical layout of the three compared configurations is provided in Figure 4.2. Two of the configurations are double Bracewell nullers, namely the linear and the rectangular designs, they are detailed in subsection 4.3.1. The Kernel nuller uses a different beam combination strategy, which will be detailed in subsection 4.3.2.

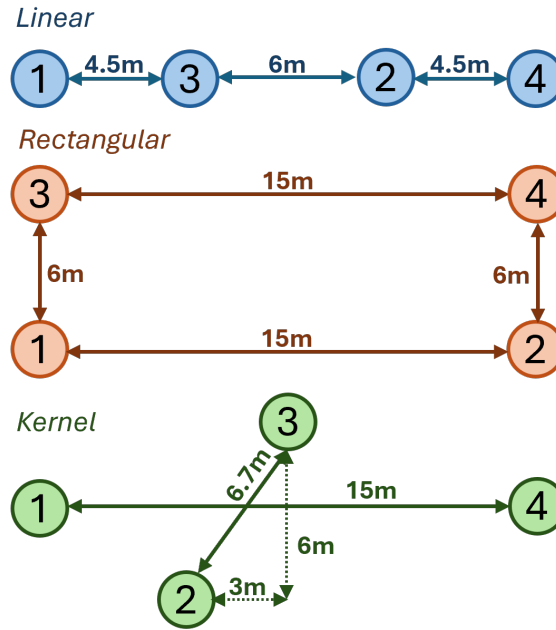


Figure 4.2: Sketch of the relative array positions of the architectures compared in this study.

4.3.1. The double Bracewell nullers

The only difference between the linear setup and the rectangular setup in this comparison is relative position of the telescopes, the actual nulling steps are the same. In practice the telescope positions will also have an impact on the eventual optical and mechanical designs, however these are still unknown and thus beyond the scope of this research.

In a double Bracewell nuller the beams are nulled in two steps: first a π phase shift is applied to two of the beams leading to two bright outputs and two dark outputs. These dark outputs are then recombined leading to the final differential transmission maps. Using the matrix description from section 4.2, this beam combination can be summarized using Equation 4.1. From Figure 4.2 the nulled inputs are therefore array pair 1-2 and 3-4.

$$U_{DB} = \begin{bmatrix} \frac{\sqrt{2}}{2} & \frac{\sqrt{2}}{2} & 0 & 0 \\ 0.5 & -0.5 & -0.5i & 0.5i \\ 0.5 & -0.5 & 0.5i & -0.5i \\ 0 & 0 & \frac{\sqrt{2}}{2} & \frac{\sqrt{2}}{2} \end{bmatrix} \quad (4.1)$$

A visual representation of the outputs, in a complex matrix plot (CMP), can be found in Figure 4.3. The first and last row of the combination matrix in Equation 4.1 correspond to the top left and bottom right outputs in Figure 4.3, both showing the bright outputs, where the light of the star is constructively interfered, and are therefore discarded for the nulled signal extraction. In the second step the two dark outputs, forming the middle rows in Equation 4.1 and the top right and bottom left outputs in Figure 4.3, are subtracted to create the differential, or also known as the kernel output. This subtraction is described in the kernel matrix K,

$$K = [0 \quad 1 \quad -1 \quad 0] \quad (4.2)$$

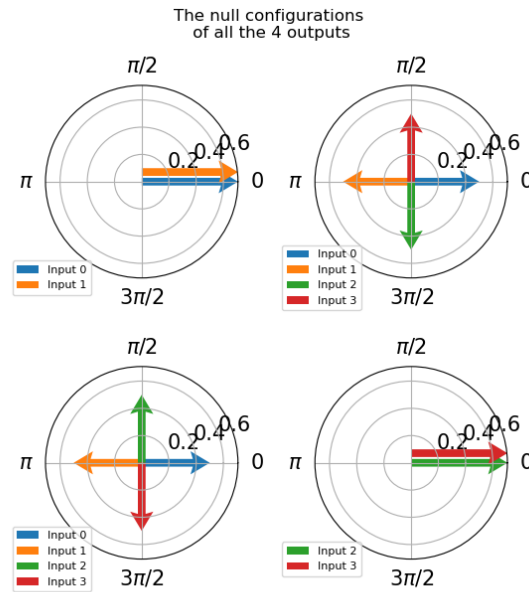


Figure 4.3: CMP of the operations described by the combination matrix for the double Bracewell nuller. The bright outputs are displayed in the top left and bottom right corners, while the two others show the dark outputs. The arrows display the contribution of the inputs at each of the outputs.

The outputs of the described nulling steps can also be visualized by showing the transmission map at each output. From the first nulling step four the outputs for the linear configuration are shown in Figure 4.4 and for the rectangular in Figure 4.5. Here the effect of the array geometry again becomes clear. Despite the outputs being generated in the exact same way the resulting pattern in the transmission map shows the distinction between these two arrays. The two dimensional nature of the rectangular configuration also shows fringe formation in two dimensions.

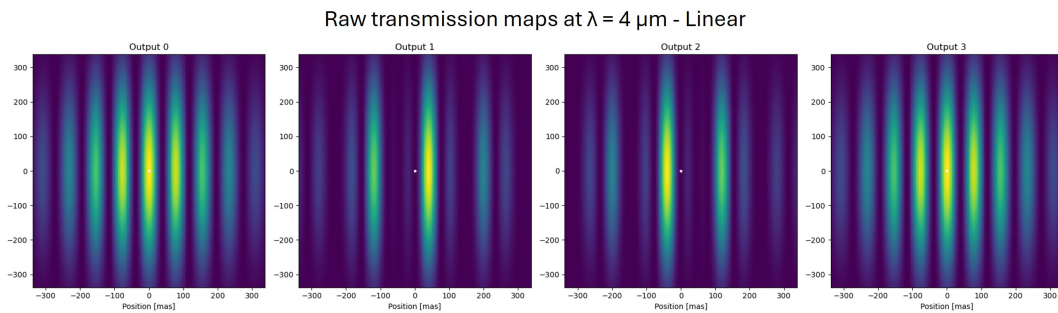


Figure 4.4: Transmission map after first nulling step of the linear double Bracewell configuration. Output 0 and 3 show the bright outputs and output 1 and 2 the dark outputs.

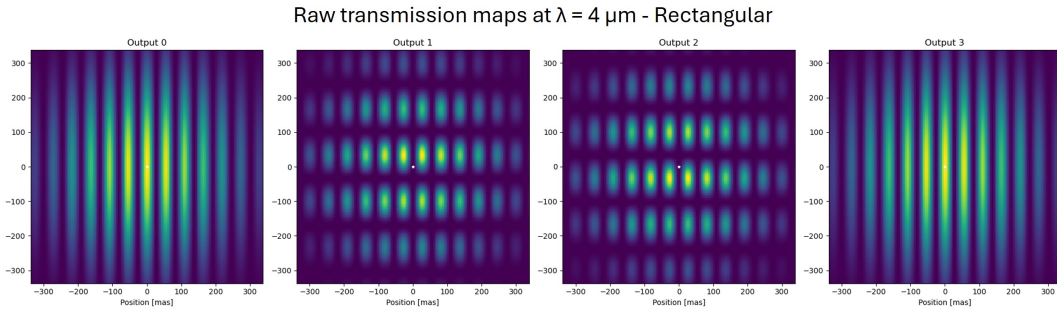


Figure 4.5: Transmission map after first nulling step of the rectangular double Bracewell configuration at wavelength bin $4 \mu\text{m}$. Output 0 and 3 show the bright outputs and output 1 and 2 the dark outputs.

In the second nulling step the dark outputs are combined to generate the differential output, described by the Kernel matrix. The corresponding differential transmission maps are shown in respectively Figure 4.6 for the linear configuration and Figure 4.7 for the rectangular array.

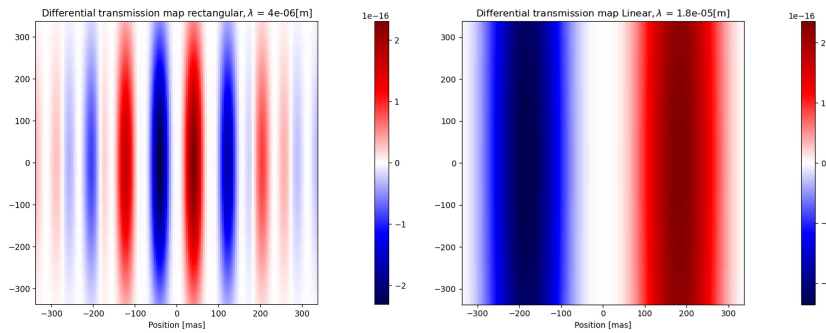


Figure 4.6: Differential transmission map of the linear double Bracewell configuration. The two outer spectral bins are displayed to show the scaling of the transmission map. The negative values in the transmission map originate from the subtraction of the dark outputs. The coloring indicates the number of photons/ s/m^2

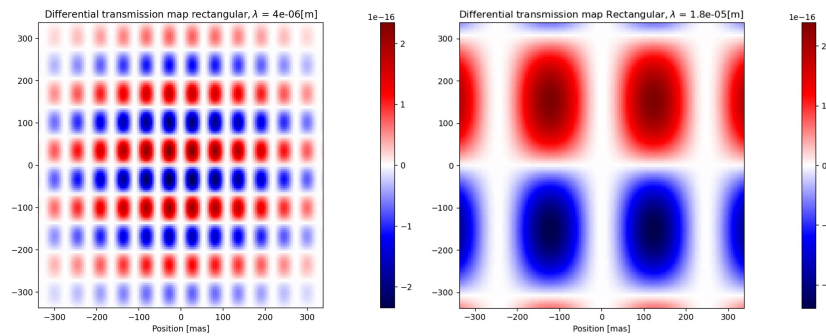


Figure 4.7: Differential transmission map of the rectangular double Bracewell configuration. The two outer spectral bins are displayed to show the scaling of the transmission map. The negative values in the transmission map originate from the subtraction of the dark outputs. The coloring indicates the number of photons/ s/m^2

The differential outputs are also sometimes referred to as the kernel outputs and it is from this combined transmission map that the final signal is obtained. The interferometer is rotated around the line of sight to create a modulation in the intensity as the planet moves through the map. To illustrate the signals behavior throughout the different spectral channels the no noise modulations for a planet located at $[0, 100]$ is shown in Figure 4.8. When a measurement is made by the instrument, the goal is to retrieve the modulation pattern that is most likely to correspond to the observed system from the noisy data.

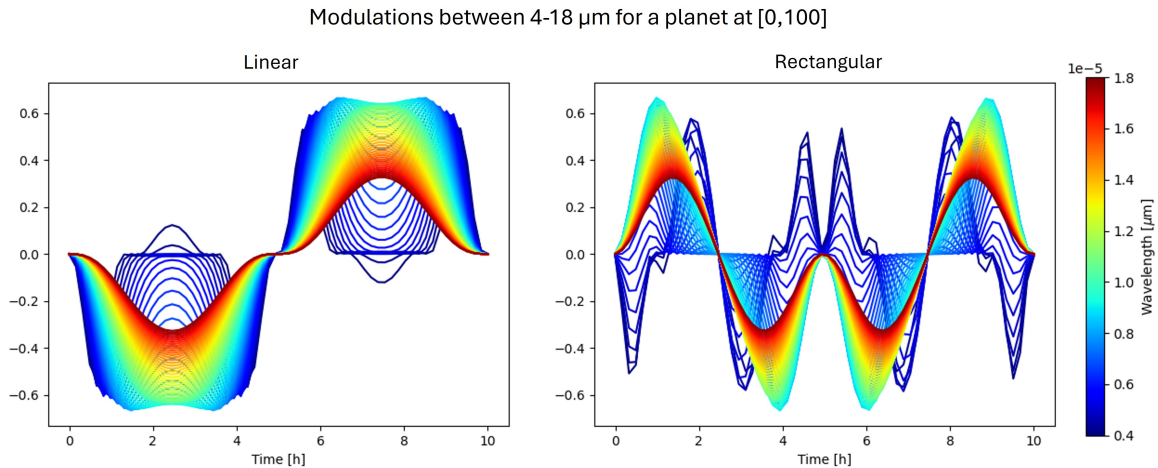


Figure 4.8: Modulations of the linear (left) and rectangular (right) double Bracewell configurations at each spectral channel for a planet located at [0,100] mas in the differential transmission map.

4.3.2. The Kernel configuration

The idea for a kernel nuller originated from the desire to have a stable null depth. In Figure 4.9, the modeled variation in null-depth as the result of an applied piston for a 'standard' four aperture nuller with 3 dark outputs can be found [28]. The dashed line shows the predicted value of the null depth. During the observation the majority of the time the null depth is not exactly what it is expected to be and instead shows a wide distribution. On top of this, the null depth does not follow a normal distribution but instead is skewed. This makes predicting the null depth difficult and therefore more computationally expensive.

Due to this imperfect behavior of the null depth the idea was that it might therefore be more advantageous to design for a more sub-optimal case, which occurs more frequently, compared to an ideal case which in reality is seldom achieved [28], by creating a more robust observable, the kernel null. The name kernel is a reference to kernel phases, a robust observable commonly used in stellar interferometry.

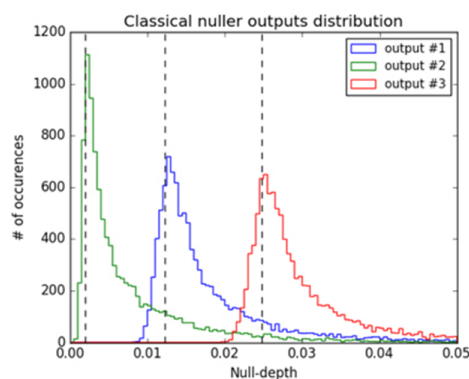


Figure 4.9: The distribution of the nuller outputs after a single nulling step during the observation of a binary object with a modeled 50 nm RMS residual piston excursion. The dashed line displays the expected null location. [28]

A kernel nulling interferometer has two stages. A simplified schematic overview of the stages in the nuller can be found in Figure 4.10. This example shows a four telescope setup used in this research, however it is possible to scale the concept to an arbitrary number of collecting telescopes [20].

The four light beams enter the system on the left hand side and will be combined as a conventional nuller would in the first stage, labeled N in the figure. In this case this is a 4x4 coupler, which means

the four incoming beams will also be transferred to four outputs: one bright output in which the star light is focused and three dark outputs that will be used to find potential off-axis sources.

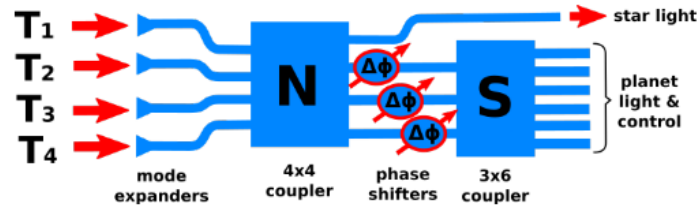


Figure 4.10: Schematic overview of a four beam Kernel nullo, where N is the first coupler and S the second coupler. The light enters the four telescopes labeled T# on the left of the figure. After the two stages the output consists of a bright output with the focused starlight and six nulled outputs [28].

The functionality of this first stage is described by the matrix N , [20]:

$$N = \frac{1}{\sqrt{4}} \begin{bmatrix} 1 & 1 & 1 & 1 \\ 1 & 1 & -1 & -1 \\ 1 & -1 & 1 & -1 \\ 1 & -1 & -1 & 1 \end{bmatrix}$$

The CMP representation is shown in Figure 4.11. Here the constructive output is indexed as Output 0, and will no longer be used in the second stage. The other three outputs follow from the pairwise combination described by matrix N. It can be seen that all outputs are aligned with the real axis and have no imaginary components at this stage.

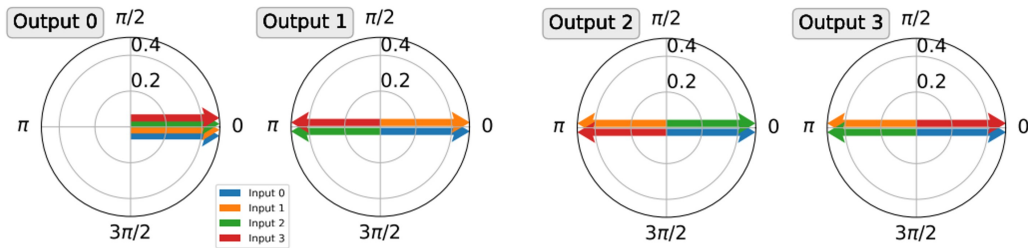


Figure 4.11: CMP of the operations described by the combination matrix, N, for the kernel nullo after the first stage [20]

In the second stage the three dark output beams from the first stage are recombined in a 3x6 coupler which applies a $\frac{\pi}{2}$ phase shift, leading to 6 dark outputs. The functionality of this second stage can be modeled using matrix S.

$$S = \frac{1}{\sqrt{4}} \begin{bmatrix} 1 & e^{i\frac{\pi}{2}} & 0 \\ e^{i\frac{\pi}{2}} & 1 & 0 \\ 1 & 0 & e^{i\frac{\pi}{2}} \\ e^{i\frac{\pi}{2}} & 0 & 1 \\ 0 & 1 & e^{i\frac{\pi}{2}} \\ 0 & e^{i\frac{\pi}{2}} & 1 \end{bmatrix}$$

The total beam combination can be summarized using Guyon's matrix model in Equation 4.3, and visually in Figure 4.12. It can be seen that due to the phase shift, the outputs now contain an imaginary component in combination with a real component. Each of the output pairs (1-2, 3-4, 5-6) is a mirror image of the other. Comparing with Figure 4.11, it can be observed that the amplitude of the outputs

have been reduced as a result of splitting the signal into additional outputs.

$$U_{ker} = \begin{bmatrix} \frac{1}{2} & \frac{1}{2} & \frac{1}{2} & \frac{1}{2} \\ \frac{\sqrt{2}}{4} & -\frac{\sqrt{2}i}{4} & -\frac{\sqrt{2}}{4} & \frac{\sqrt{2}i}{4} \\ \frac{\sqrt{2}}{4} & \frac{\sqrt{2}i}{4} & -\frac{\sqrt{2}}{4} & -\frac{\sqrt{2}i}{4} \\ \frac{\sqrt{2}}{4} & -\frac{\sqrt{2}}{4} & -\frac{\sqrt{2}i}{4} & \frac{\sqrt{2}i}{4} \\ \frac{\sqrt{2}}{4} & -\frac{\sqrt{2}}{4} & \frac{\sqrt{2}i}{4} & -\frac{\sqrt{2}i}{4} \\ \frac{\sqrt{2}}{4} & \frac{\sqrt{2}i}{4} & -\frac{\sqrt{2}}{4} & -\frac{\sqrt{2}i}{4} \\ \frac{\sqrt{2}}{4} & -\frac{\sqrt{2}i}{4} & \frac{\sqrt{2}}{4} & -\frac{\sqrt{2}i}{4} \\ \frac{\sqrt{2}}{4} & -\frac{\sqrt{2}i}{4} & \frac{\sqrt{2}i}{4} & -\frac{\sqrt{2}}{4} \end{bmatrix} \quad (4.3)$$

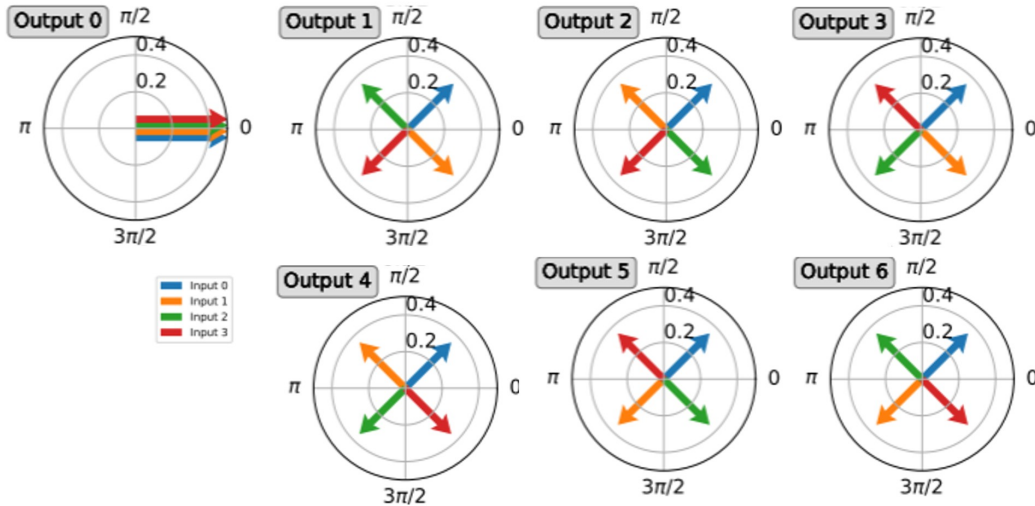


Figure 4.12: CMP of the operations described by the full combination matrix of the kernel nuller. Output 0 showing the bright output and the other diagrams displaying the 6 dark outputs.

It is from these six final dark outputs that the kernels can be found. For this design the centro-symmetric signal can be eliminated simply by performing a pairwise subtraction of the outputs. Leading to kernel matrix K in [28].

$$K = \begin{bmatrix} 1 & -1 & 0 & 0 & 0 & 0 \\ 0 & 0 & 1 & -1 & 0 & 0 \\ 0 & 0 & 0 & 0 & 1 & -1 \end{bmatrix} \quad (4.4)$$

To demonstrate the described steps with the transmission maps, like was done in subsection 4.3.1, the raw outputs after the first stage N are shown in Figure 4.13.

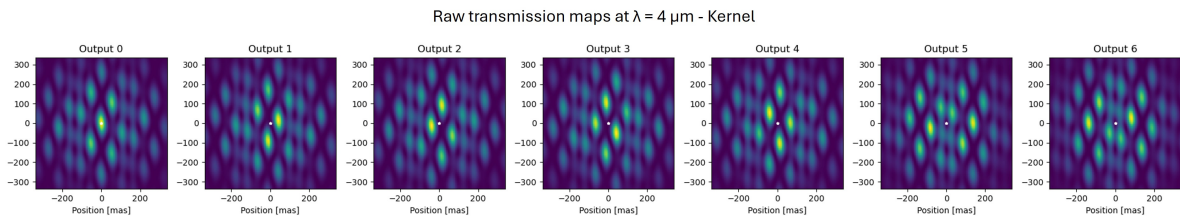


Figure 4.13: Transmission maps of the six dark outputs of the 4 telescope Kernel configuration at wavelength bin $4 \mu\text{m}$. Output 0 shows the bright output and the other six represent the dark outputs.

After the pairwise subtraction as described by Equation 4.4 the resulting differential outputs are shown in Figure 4.14. The three generated kernel outputs are all independent. The kernel nuller produces more observables compared to the double Bracewell's, however the quality of these observables is impacted by the splitting of the signal. The central question raised is whether or not these additional observables will also lead to a better performance in constraining the planetary parameters.

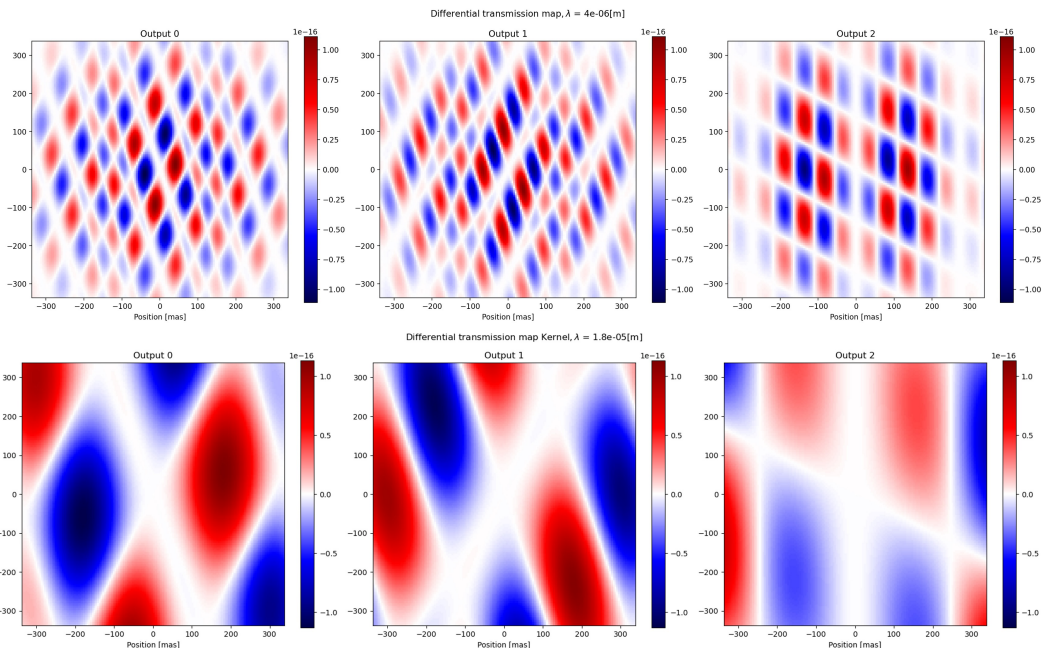


Figure 4.14: Differential transmission maps of the kernel configuration. Contrary to the double Bracewell design the kernel produces three sets of differential outputs and therefore also generates three signals. The coloring indicates the number of photons/s/m²

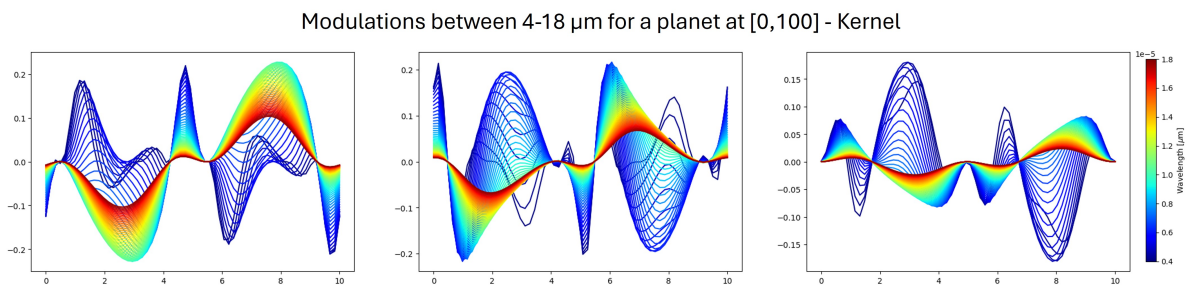


Figure 4.15: Modulation signals for all spectral bins for the kernel setup as created by a planet at location [0,100] in the transmission maps.

5

SCIFYsim

The three compared architectures were simulated using the pre-existing simulator SCIFYsim. SCIFYsim is a python module that can be used to model high-contrast interferometric instruments and was originally developed for ground based observations at the VLTI as part of NOTT. This chapter will briefly describe how the simulator works and how it was adapted for this research.

5.1. Initializing a simulation in SCIFYsim

To start a new simulation the user changes the inputs for their observation objective in the configuration file. This file contains all the data required to simulate the observation. This includes information about the observatory location and geometry, the observed target, the observation and sampling itself, the instrumental parameters, and due to its original application for ground based observations also the atmospheric characteristics.

All this data is gathered from the configuration file and stored in the simulator object, referred to as 'asim'. This is the object containing the simulation information and is called by the user to both configure the computations and extract data. To give a concrete idea of some of the functionalities that can be called by the user using the asim object please refer to Table 5.1, where a small selection of options is displayed. After the simulator object has been initialized the user can generate the transmission map data associated with the combiner and use the plot tools in SCIFYsim to visualize them.

SCIFYsim function	Returns
<i>Accessing simulation data</i>	
asim.lambda_science_range	Returns an overview of the wavelength bins used for the observations
asim.combiner.M	Returns the combination matrix according to Guyon's model
asim.combiner.K	Returns the kernel matrix K used to create the kernel outputs
asim.target	View target information
asim.obs	View information about the observatory used
<i>Initializing a simulation</i>	
asim.point	Point the array towards the target and update the combiner
asim.make_metrologic_exposure	Simulate an exposure of the target on the detector
asim.build_all_maps	Generate transmission maps for each wavelength channel and observation epoch.

Table 5.1: A selection of functions within SCIFYsim that may be accessed by the user in order to interact with the simulation object.

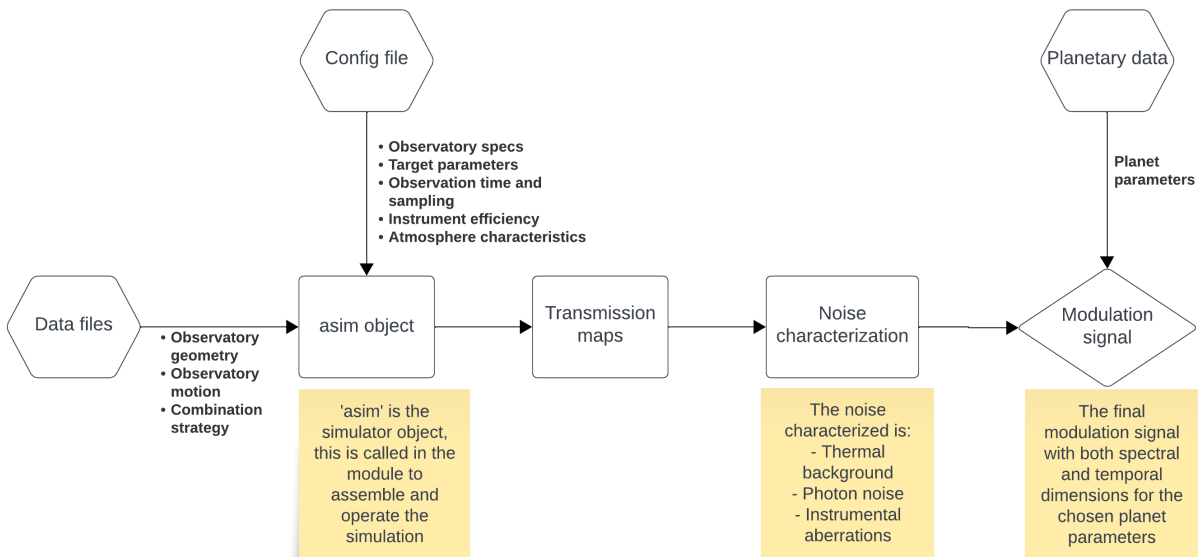


Figure 5.1: Block diagram showing the main steps of SCIFYsim used in this research. The user modifies inputs using the configuration file and interacts with the simulator via the simulator object.

5.2. Modifications to SCIFYsim

SCIFYsim was originally developed for ground based observations. Application to a space environment therefore required some tuning in the atmospheric parameters in the configuration file to remove these effects as much as possible.

Additionally, the provided code to interact with the simulator was not yet fully compatible with the kernel configuration. The issues were mostly related to the fact that a double Bracewell usually outputs a single differential, or kernel, null. However, for the chosen kernel setup the outputs lead to three independent differential nulls therefore adding another dimension to the outputs generated. This involved expanding the plotting features to generate three individual plots for the results and updating matrix transformations to be generalized to deal with varying matrix dimensions.

Finally, in the final stages the model was expanded to deal with multiple planets in the system. This update required expansions in the SCIFYsim code itself related to the functions which generate the source from the input parameters. In the updated version the planet sources are made iteratively and are stored, to be summed together for the generation of the final signal. The expansion has been implemented in such a way that an arbitrary number of planets could hypothetically be generated, however within the scope of this research only two planet models were employed.

5.3. Generating the noisy signals

In section 2.5 it was explained how the differential transmission maps lead to the signal that is created by a planet being present. Like shown in chapter 4, the signals are different for each of the configurations and importantly have a large spectral variation. To help visualize the model steps, the example below will use a simplified case at just one spectral channel in Figure 5.2. This example is at the spectral channel with a high Signal to Noise Ratio (SNR). However it is important to keep in mind that there are also many spectral channels, especially at lower λ , where the noise dominates the signal more. For the two planet system the contributions from the individual planets are summed together, before the noise is added.

From the transmission maps and the inputted planetary position at each spectral channel a no noise signal shown on the left panel in Figure 5.2 is obtained. To characterize the noise associated with the observation a baseline observation is performed for a system without any planets. By performing a series of 'observations' on the selected target star without any planet signal, the exposure on the detector can be stored to record the expected noise in the system.

This recorded data set is then expanded using bootstrapping to generate additional samples for the

noise levels. Bootstrapping creates new datasets from a recorded dataset by randomly resampling from the original set. From this estimated noise distribution it is possible to determine the covariance matrix of the instrument. This information is in turn used to draw a signature of the noise that is added onto the signal. This step is shown in the middle panel in Figure 5.2.

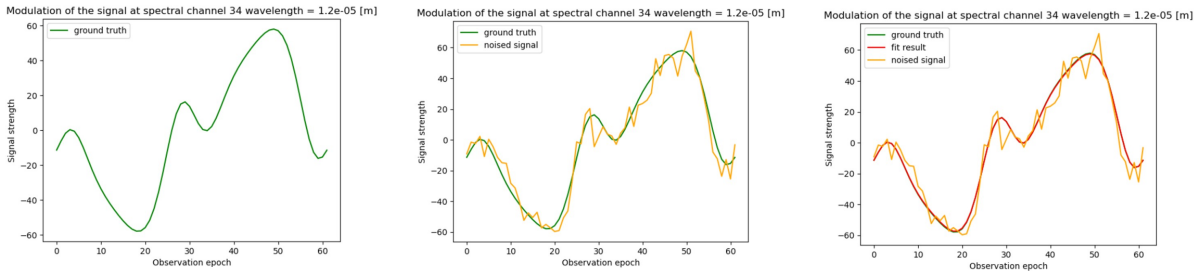


Figure 5.2: Example of the retrieval process of the model at $\lambda = 12 \mu\text{m}$. On the left the planet signal is shown with no noise applied, in the middle the orange line shows the noisy signal that is fed to the fitter on the right a successful fitting is observed.

5.4. Retrieving planetary parameters

The final step in the model is to retrieve the actual planetary parameters from the noisy signal, shown in the third step in Figure 5.2. To do this in the code, the Non-Linear Least-Squares Minimization and Curve-Fitting for Python (LMFIT) python module was used [29]. The module has been developed for the fitting of complex models for non-linear least-squares problems. Compared to other libraries it simplifies keeping track of the variables in the fitting by using a Parameter object which can be defined by the user.

In the code this Parameter object needs to be defined to specify the variables that can be changed by the fitter. The planets were simulated with four planetary parameters summarized in Table 5.2. Together with the parameters, the asim object is fed to the fitter, so that it can recreate the modulation signal with the same instrumental parameters. The fitter then tries to match the original signal by varying the planetary parameters.

Table 5.2: The planetary parameters used in the model. A source is inputted by these four characteristics and at the end the model outputs the performance of retrieving these.

Parameter	Symbol	Unit	Description
Radius	R	R_e	The radius of the planetary body
Temperature	T	K	The (black body) temperature of the planet
Separation	Sep	mas	The angular separation between the star and the planet
Position Angle	PA	deg	The planet's angle with the vertical axis in a face-on view

A summary showing the process used to generate and consequentially fit the planet signal is shown in the block diagram in Figure 5.3. For the single planet case an Markov Chain Monte Carlo (MCMC) simulation was used to sample the posterior distribution of the parameters. The MCMC was used to verify that the results obtained by a single iteration were not merely an accidental result. It was found that the results from this simulation matched the single fitting results closely in cases of high SNR and were therefore not implemented in later stages to save computational costs for the simulations.

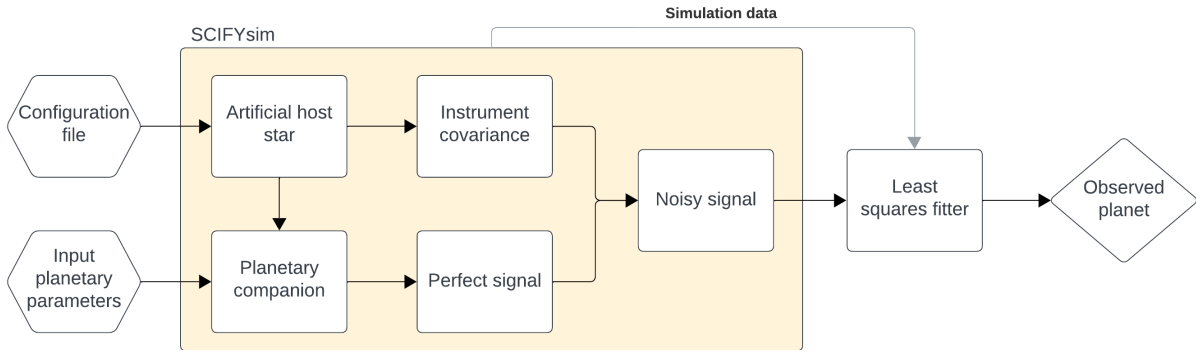


Figure 5.3: Block diagram of the fitting process in SCIFYsim from the input of the planetary parameters to the retrieval from the noisy signal. The yellow box shows the functionalities which are part of SCIFYsim.

5.5. Origin and impact of correlations

From the fitting process the estimated values for the parameters are returned together with the associated uncertainties. The LMFIT library also returns the strength of the correlations between each parameter pair. In most research related to the performance of a nulling interferometer the planet yield is used as the performance metric, [37, 32], which tends to neglect the presence of correlations that may be encountered.

Some correlations occur as a direct result of the chosen model, for example using the black body spectrum to model the flux a direct link between the radius and temperature is introduced. For the other parameters however the correlation origin is less obvious. The encountered correlations can be split into two categories temporal correlations and spectral correlations.

The temporal correlations are not modeled in SCIFYsim, however they do occur in practice. They occur due to time-dependent variations between the measurements, for example as a result of slow vibrations in the spacecraft. In this research it is assumed that all the vibrations present are shorter than the detector integration time and that the observation samples are all independent.

The spectral correlations are modeled during the characterization phase of the noise. In SCIFYsim these spectral correlations originate due to user inputted OPDs between the beams. These OPDs introduce a spectrally dependent phase shift, described in Equation 5.1. It was demonstrated in chapter 4 that the transmission maps of the instruments are spectrally dependent and therefore these phase shifts will also leak into the final results.

$$\Delta\phi = \frac{2\pi}{\lambda} \Delta s \quad (5.1)$$

Part II

Scientific Paper

Constraining exoplanet parameters in nulling interferometry

A configuration comparison study for a single spacecraft mission

L. Greijn¹

Faculty of Aerospace Engineering, Delft University of Technology

ABSTRACT

Context. In preparation of a large-scale nulling interferometry mission aiming to detect and characterize Earth-like exoplanets, it is required that key technologies are demonstrated in a space environment. Design trade-offs for a large mission have assumed long, reconfigurable baselines. However, it is uncertain that the same design performs best for a smaller mission with shorter, fixed baselines. *Aims.* This research aims to compare the performance of three possible nulling configurations, a linear double Bracewell, a rectangular double Bracewell and a off-center kite shaped kernel nuller, on their ability to constrain the temperature, radius, and position of an exoplanet during the mission detection phase.

Methods. The configurations are compared by planetary signal simulations performed using the simulation software SCIFYsim. The configurations are compared based on three categories (1) performance for a single planet case, (2) the introduced correlations between planetary parameters, and (3) the performance in a two planet case.

Results. The analysis indicates that the configurations performed similarly when modeling a single planet system, with the linear configuration showing a slight advantage. Regarding the parameter correlations, the kernel configuration exhibits the least correlations between fitted parameters. In the two-planet system, both the rectangular and kernel configurations achieve the highest accuracy in retrieving planetary parameters, though the overall performance remains relatively similar across configurations. Notably, despite the blurry signature of the two planet system in the matched filter map for the linear configuration, the fitting process is able to retrieve the planetary parameters.

Key words. Nulling interferometry – Kernel nulling – Double Bracewell – SCIFYsim

1. Introduction

The Large Interferometer for Exoplanets (LIFE; Quanz et al. 2022) is a mission initiative currently under development. The goal of LIFE is to detect and characterize terrestrial exoplanets, potentially answering long standing questions on the atmospheric and surface conditions of exoplanets. To characterize these distant worlds it is of interest to observe them in the mid-infrared (MIR) wavelength. This domain allows the determination of the planet’s temperature and radius, needed to infer the planet density and to make preliminary characterizations of its atmosphere Tacconi et al. (2021). Additionally, a number of Earth’s atmospheric molecules show absorption bands within this wavelength range.

To address the key challenges of direct detection of the thermal emission, namely achieving high contrast and high angular resolution, LIFE employs nulling interferometry. Nulling interferometry is a technique that is used to cancel, or null, the light of a star, to reveal a faint nearby planet. This is achieved by interferometric combination of the incoming light in such a way that the stellar light is destructively interfered, while catching a potential faint planet in a constructively interfered region (Bracewell 1978). With nulling interferometry the requirements on the telescope size are relaxed compared to other high contrast methods, such as the use of a coronagraph.

The LIFE mission concept involves a constellation of five formation-flying spacecraft: four to collect incoming photons and one to combine the light beams (Dannert et al. 2022). Before such an ambitious large-scale mission can be realized it is critical to demonstrate key technologies. Currently there are

ongoing developments for a single-spacecraft precursor demonstrating the use of space-based nulling interferometry for the detection of exoplanets. The boundary parameters for the mission have been established, however the configuration of the collecting telescopes and the beam combination strategy remain under evaluation (Loicq et al. 2024).

Following from the legacy of previous space-based nulling interferometry proposals, like Darwin (Leger & Herbst 2007) and Terrestrial Planet Explorer Interferometer (TPF-I) (Beichman et al. 2006; Lawson et al. 2008), the leading design suggestion tends to be a rectangular double Bracewell configuration (Lay & Dubovitsky 2004; Dannert et al. 2022). In this geometry the telescopes are placed in a rectangle creating two sets of baselines, the longer, imaging, baseline that can be used for high resolution interferometry and the shorter, nulling, baseline, that can be used to null the stellar light (Glauser et al. 2024). Using this architecture the 4 beams collected by the telescopes are combined into four outputs, two bright outputs in which the stellar light is focused and 2 dark outputs which are used for exoplanet observations.

This rectangular double Bracewell is the leading design for a free flying configuration, in which the baselines can be re-configured. However, the question arises if this result holds true for a fixed setup with much shorter baselines. Over the decades since the first proposal by Bracewell (1978) a number of alternative configurations have been proposed. Examples include the linear double Bracewell configuration (Angel & Woolf 1997), in which the collecting telescopes are arranged in a linear fashion, and more recently, a novel approach known as kernel

nulling (Martinache & Ireland 2018). Kernel nulling can be used for any number of collecting apertures (Laugier et al. 2020), but its effectiveness relies on non-redundant baselines, favoring non-symmetric layouts.

This study aims to address the question: how does a single spacecraft four-telescope kernel nuller compare to a linear and rectangular double Bracewell configurations in providing constraints on top-level planetary parameters during the detection phase of a space-based nulling interferometry exoplanet finding mission? The comparison will be performed using computational simulations. The evaluation of the performance is based on three criteria; (1) single planet performance, (2) the correlation levels between the planetary parameters and (3) the performance when expanding to a two-planet system.

2. Methodology

To simulate the configurations SCIFYsim (Self-Calibrated Interferometry For exoplanet spectroscopy) was employed. SCIFYsim is a python module designed to simulate nulling interferometers. It was originally developed for applications in the development for instruments at the Very Large Telescope Interferometer (VLTI), however it can also be applied to alternate instruments (Laugier et al. 2021). SCIFYsim employs an integrated approach that combines multiple models to simulate the systems. This section will first provide an overview of the models used by SCIFYsim and, following this, the setup of the tested cases will be discussed.

The global parameters of the space mission used for the simulation initialization are summarized in Table 1. The analysis is performed during the detection stage of the mission, in which a limited observation time is available per observed system. A broad wavelength band, ranging from 4-18 μm , is divided into 60 equally spaced spectral channels.

Table 1. Mission parameters used in the configuration of the simulator for the single spacecraft testbed

Parameter	Value
Aperture diameter	2m
Number of apertures	4
Maximum spacecraft length	15m
Spacecraft rotation rate	$1.745e^{-4}$ rad/s
Total instrument throughput	5%
Spectral range	4 – 18 μm
Number of spectral bins	60

The observation parameters shown in Table 2 were used in the initialization, it is assumed the observed system has a sun-like host star. The observation duration of 10 hours in combination with the rotation rate of the spacecraft, means that one full spacecraft rotation is made during the observation.

2.1. Modeling the nulling interferometers

With these global mission parameters the individual configurations can be modelled. This section will discuss how the nulling process is modeled within SCIFYsim.

Table 2. Observation parameters used in the SCIFYsim simulations. The simulated host star is a sun-like star at a distance of 10 pc. The observations are assumed to take place in the detection stage of the mission.

Parameter	Value
Observation duration	10 h
Observation date & time	2020-10-20, 00:00
Observation samples	62
Distance to planetary system	10 pc
Temperature host star	5772 K

2.1.1. Array geometries

In a nulling interferometer the system response used to block the stellar light is a directly related to the relative position of the collecting apertures. A description of the individual system responses will be discussed in 2.2. A sketch of the geometrical layout of the three compared configurations is provided in Figure 1.

Each of the configuration has a maximum length of 15 meters, and features multiple baseline pairs which are combined to generate the outputs. In Figure 1, the baseline pairs for the linear and rectangular double Bracewell configurations are 1-2 and 3-4. For the kernel configuration all baselines are used in the nulling process. In this work the possible mechanical and optical implications of a chosen geometry, such as stiffness and the optical train design are neglected in the comparison. The configurations are analyzed solely from a signal based perspective.

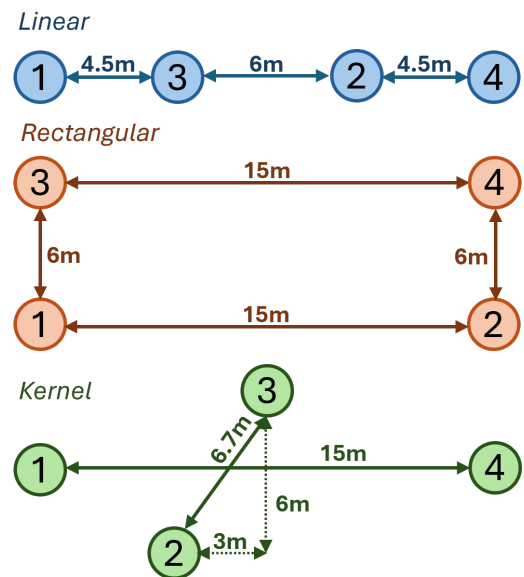


Fig. 1. Geometrical layout of the apertures, from top to bottom linear double Bracewell (blue), rectangular double Bracewell (red), and kernel (green). The baselines are measured from the center of each aperture.

2.1.2. Beam combination

The beam combination of the instruments is modeled in SCIFYsim using a matrix-based approach, first introduced by Guyon

et al. (2013), a detailed description of his model can be found in part I of the thesis in Section 4.2. In Guyon's model the operations of the nuller are modeled by linear combinations of the input vector V , where V represents the complex amplitudes at the entrance of the system. The combinations linking the inputs V to the outputs W , and thus the operations of the nuller, are documented in matrix U or simply

$$W = UV \quad (1)$$

It is important to note that in this relation U is independent of the geometric positions of the apertures, which are incorporated in matrix V . The detector recording the measurements registers the intensity, I , where $I = |W|^2$. It is the modulation of this intensity value over time which is used to reconstruct information about the observed planetary system. Due to the independent nature with respect to the array geometry both double Bracewell architectures (linear and rectangular) are described by the same combination matrix U_{db} .

$$U_{db} = \begin{bmatrix} \frac{\sqrt{2}}{2} & \frac{\sqrt{2}}{2} & 0 & 0 \\ 0.5 & -0.5 & -0.5i & 0.5i \\ 0.5 & -0.5 & 0.5i & -0.5i \\ 0 & 0 & \frac{\sqrt{2}}{2} & \frac{\sqrt{2}}{2} \end{bmatrix} \quad (2)$$

From matrix U_{db} it follows that the double Bracewell designs have two bright outputs, the top and bottom row, in which the stellar light is interfered constructively and two dark outputs, described by the middle rows, from which the planet information can be reconstructed. These two dark outputs are recombined in order to create a single differential output and therefore lead to only one observed signal.

The kernel design used in this work is a 4x7 combiner, where the four input beams are combined into seven outputs and instead of two dark outputs in generates six. Its operation can be described using matrix U_{ker} shown below. These six dark outputs can be recombined into three independent differential outputs.

$$U_{ker} = \begin{bmatrix} \frac{1}{2} & \frac{1}{2} & \frac{1}{2} & \frac{1}{2} \\ \frac{\sqrt{2}}{4} & -\frac{\sqrt{2}i}{4} & -\frac{\sqrt{2}}{4} & \frac{\sqrt{2}i}{4} \\ \frac{\sqrt{2}}{4} & \frac{\sqrt{2}i}{4} & -\frac{\sqrt{2}}{4} & -\frac{\sqrt{2}i}{4} \\ \frac{\sqrt{2}}{4} & -\frac{\sqrt{2}}{4} & -\frac{\sqrt{2}i}{4} & \frac{\sqrt{2}i}{4} \\ \frac{\sqrt{2}}{4} & -\frac{\sqrt{2}}{4} & \frac{\sqrt{2}i}{4} & -\frac{\sqrt{2}i}{4} \\ \frac{\sqrt{2}}{4} & \frac{\sqrt{2}i}{4} & -\frac{\sqrt{2}i}{4} & -\frac{\sqrt{2}}{4} \\ \frac{\sqrt{2}}{4} & -\frac{\sqrt{2}i}{4} & \frac{\sqrt{2}}{4} & -\frac{\sqrt{2}i}{4} \end{bmatrix} \quad (3)$$

2.2. Transmission maps

Guyon's model separates the geometry and beam combination elements of the instrument, so that they may be optimized separately. However, it is their combined effect which determines the overall performance. This combined effect can best be shown in the transmission map, which displays the transmission pattern created by the beam combination mapped on the sky plane. It can be thought of as a sieve that filters the photons that reach the detector.

The differential transmission map for the linear configuration is displayed in Figure 2. The two dark outputs from the combination are recombined into this single differential map by a pairwise combination, leading to negative values in the map. The

observed target star is located in the central null on the optical axis at $[0,0]$. It is important to note that the transmission maps have a spectral dependence and will scale as a function of the wavelength. Therefore the interferometer has different sensitivity regions in the field plane depending on the spectral regime, the impact of this will be discussed in Section 2.3. Additionally, as the spacecraft rotates, so will the transmission map. It is this rotation which creates the a modulated signal that used to find the planets. For this linear array this modulation pattern will therefore have a sine-like path.

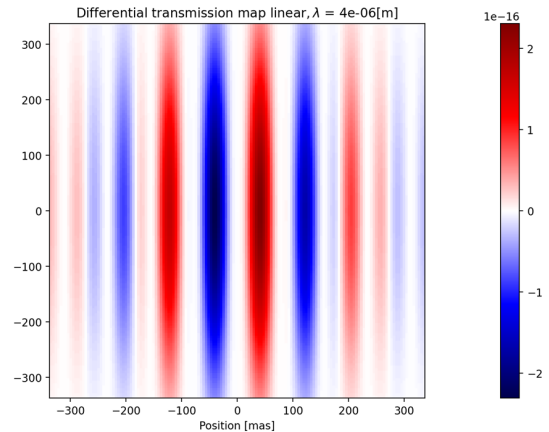


Fig. 2. Differential transmission map for an on sky view of 600 by 600 mas of the linear double Bracewell architecture at spectral bin $\lambda = 4 \mu\text{m}$. The color mapping shows the transmission in ph/s/m^2 . The negative values originate from the subtraction of the two dark outputs.

The transmission map of the rectangular double Bracewell is displayed in Figure 3. The two-dimensional nature of the array is also reflected by the two dimensional spacings in the fringe pattern shown in the transmission map. In both Figure 2 and Figure 3 it can be observed that the instrument response starts to decline at the edges of the field. The field of view is limited by a single mode spatial filter, which is a part of the optical train in order to improve the quality of the wavefront and thus improve the achieved contrast Ollivier & Mariotti (1997).

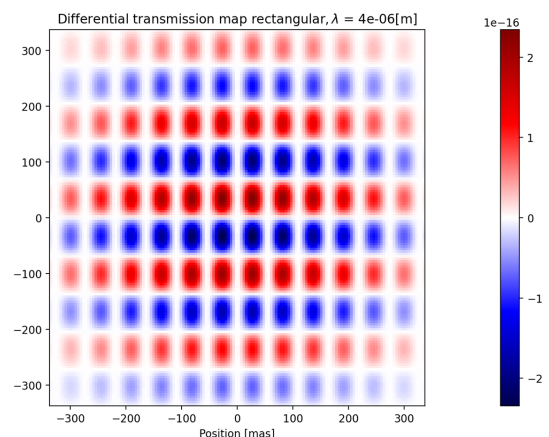


Fig. 3. Differential transmission map for an on sky view of 600 by 600 mas of the rectangular double Bracewell architecture at spectral bin $\lambda = 4 \mu\text{m}$.

Finally, the transmission maps of the kernel configuration is shown in Figure 4.

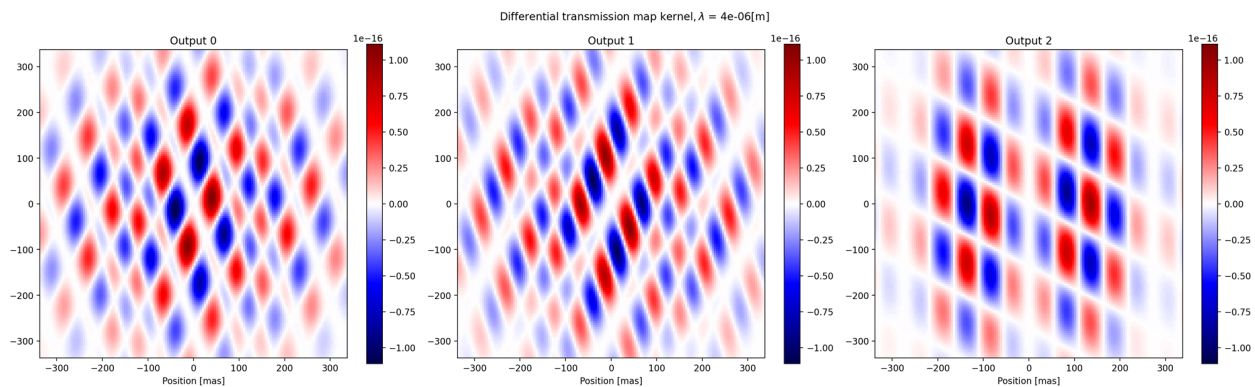


Fig. 4. Differential transmission maps for an on sky view of 600 by 600 mas of the kernel nuller at spectral bin $\lambda = 4 \mu\text{m}$. The three differential outputs show the combination of the six dark outputs. Output 0: combination of output 1-2, output 1: combination of 3-4 and finally output 2 the combination of 5-6.

The additional splitting of the signal into six dark outputs leads to three independent transmission maps. When observing a planetary system that also implies that three independent modulation signals are created during the observation. However, as the same input signal is split, the amplitude of the kernel signals will be lower compared to the same observation in a double Bracewell configuration.

With the model of the nulling interferometers established a prediction of the received signal can be made. Placing a planet at a distance of 130 mas from the star and assuming no noise is present, the hypothetical signals at the spectral channel $\lambda = 6.4 \mu\text{m}$ is shown in Figure 5.

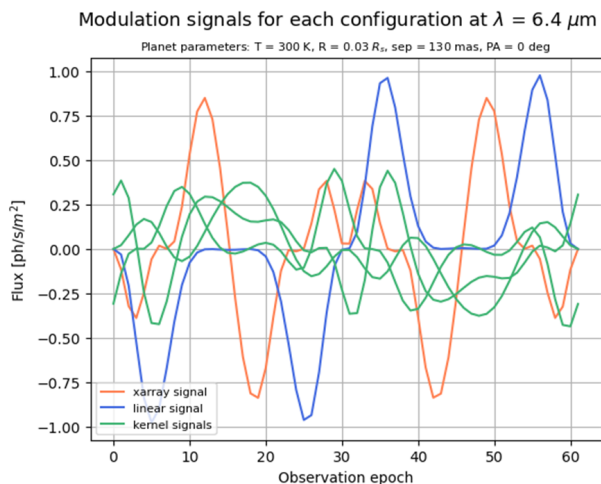


Fig. 5. The modulation signals in a noise-free case for the three configurations following from the transmission maps at spectral bin $6.4 \mu\text{m}$. The planet simulated planet is located at 130 mas from the central star with a radius of $3.3 R_e$ and a temperature of 300 K

2.3. Spectral effects

It was mentioned in 2.2 that the instruments have a variation in their sensitivity that is wavelength dependent, due to the scaling of the transmission maps. The impact of this scaling is significant as a result of the relatively broad spectral range used for the mission. The impact can be quantified using the modulation efficiency, which is defined as the absolute value of the standard deviation of the modulation. It is analogous with the amplitude of the signal produced by a planet at a given separation from its

host star for a specific wavelength. The higher the modulation efficiency, the 'stronger' the signal produced by the planet. To show the most extreme cases, the modulation efficiency of the first and last spectral channels of the rectangular array is shown in Figure 6.

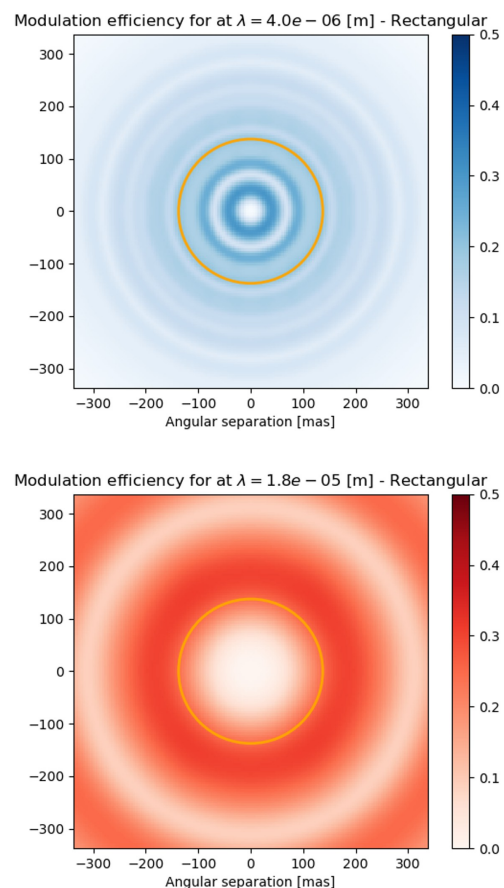


Fig. 6. Modulation efficiency of the rectangular array at $\lambda = 18 \mu\text{m}$ (red) and at $\lambda = 4 \mu\text{m}$ (blue). The orange circle displays the $\frac{\lambda}{B}$ value at $\lambda = 10 \mu\text{m}$, which can be used as the border for the sensitive region of the instrument.

From Figure 6 it can be observed that the rectangular array has some low sensitivity regions in certain spectral channels, where the signal of the planet almost disappears. These occur

due to undesirable null regions in the transmission map. The orange circle in the graph shows the separation $\frac{\lambda}{B}$ value at $\lambda = 10 \mu\text{m}$. For these configurations located at

$$\text{Sep} = \frac{10\mu\text{m}}{15\text{m}} \approx 127 \text{ mas}$$

This is the separation at which a planet will begin to create an modulation at the higher wavelength channels. It thereby indicates the minimum separation at which the full instrument becomes sensitive to planetary signals. A drawback of the broad wavelength range also comes to light when looking at Figure 6. In the region where the higher wavelengths first start to generate signal, the signal generated by the shorter wavelengths are already starting to decline.

To visualize the efficiencies of the different configurations at each spectral channel Figure 7 can be used. The curves again show the modulation efficiency as a function of angular separation, but this time all spectral channels are displayed. It is like plotting the modulation efficiency value at each spectral channel, shown in Figure 6 starting from the center of the plots, at 0 mas separation, to the edge. Due to the centrosymmetric nature of the plots this efficiency is independent of the position angle of the planet. As the separation increases, the efficiencies all start to slope downwards due to the limited field of view. The larger the surface underneath the curve, the larger the region for which the sensitivity of the instrument is maximized.

Comparing the performance of the configurations it can be observed that the rectangular array has the fastest sensitivity decline, at only one third of the efficiency in the higher spectral channels, the efficiency in the lowest channel has already reduced by about 67%. The linear and the kernel configurations have a similarly sized area underneath the graph. The linear configuration peaks higher in terms of efficiency compared to the kernel, due to the higher amplitude of the signal. However, the kernel maintains a relatively high sensitivity at each wavelength for a longer range of separations. and the drop in its performance is more gradual than those of the double Bracewell configurations.

2.4. Modeling the noise

During the journey of the signal from the planetary system to the instrument's detector, a variety of noise impacts the signal quality. In previous work extensive analysis is performed on which noise sources can be expected originating both externally and within the nulling interferometer itself (Lay 2004, 2006; Dandumont et al. 2020). The impact of the external noises, such as those generated by zodiacal effects, thermal emission, and leaking stellar flux can generally be predicted. However it is the instrument perturbations which are still a topic of uncertainty (Lay & Dubovitsky 2004).

Within SCIFYsim the following effects are modeled:

- Thermal emission and absorption of the optics
- Photon noise
- Detector noise
- Instrument perturbations, such as vibrations.

The main noise effects not modeled in the simulator are the zodiacal dust (both local and exozodiacal) and static biases or offsets that may be present in the final design. These will both have an impact on the final measurements (Defrère, D. et al. 2010; Ertel et al. 2020) and should be taken into account for more detailed design iterations.

To characterize the noise during an observation a baseline observation is made. In this observation only the star is modeled without a planetary companion. The registered 'signal' on the detector then provides an indication for the noise levels present during an observation. To provide a complete characterization the noise is resampled to provide a more robust distribution using bootstrapping (Zoubir & Iskandler 2007). This process is repeated on a series of observation frames which are assumed to be independent, and thereby temporal correlations are neglected. This registered noise distribution is summarized in the covariance matrix of the instrument. When modeling planetary systems a random draw is performed, based on the covariance level of the instrumental noise. This noise is then added onto the signal to mimic a randomized, realistic, noisy signal.

Due to the uncertainty related to the instrumental noise and the exclusion of exozodiacal effects within SCIFYsim, it is a comparison of the relative performance of the configurations which is relevant. This research does not provide absolute constraints on the instrument performance.

2.5. Modeling the planetary systems

Having characterized the instrument model, the modeling of the observed planetary systems is explored next. In SCIFYsim the planetary systems are modeled using a blackbody spectrum. From Planck's law it follows that the spectral radiance of a black body is described by

$$B_\lambda(T) = \frac{2hc^2}{\lambda^5} \frac{1}{e^{hc/\kappa\lambda T} - 1} \quad (4)$$

Where the intensity $B_\lambda(T)$ is the spectral radiance, representing the power per area per unit wavelength. T , is the temperature, h is the Planck constant, κ is the Boltzmann constant, λ is the wavelength, and c the speed of light. To find the flux received by the emitting body the spectral radiance should be integrated over the solid angle or mathematically

$$F_\lambda = \int_{\Omega} B_\lambda(T) \cos \theta d\Omega \quad (5)$$

Where F_λ is the flux for a given wavelength, Ω is the solid angle, and θ the angle the emitting body extends to relative to the optical axis. Since the observed planets located at a very large distance from the instrument and thus $R \ll D$, the relation can be written as

$$F_\lambda = B_\lambda(T) \pi \left(\frac{R}{D}\right)^2$$

Integrating over the full wavelength spectrum for a spherical surface the total power emitted reduces to Equation 6.

$$P = 4\pi R^2 \sigma T^4 \quad (6)$$

Where R is the radius of the body, T is the temperature and σ the Stefan-Boltzmann constant. In reality the power emitted by the body will be lower due to the limited wavelength range used. Despite the long distance between the instrument and the observed systems, the bodies are modeled as extended sources. instead of point sources, due to the impact their size has on the geometrical leakage through the null.

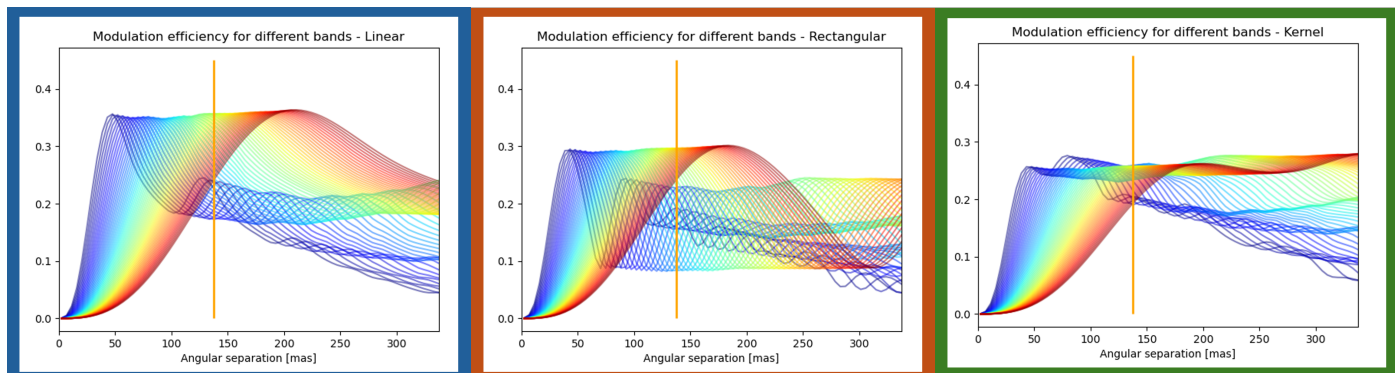


Fig. 7. Modulation efficiencies as a function of separation for each spectral channel. With the linear configuration on the left (blue), rectangular in the middle (red), and the kernel on the right (green). The orange line shows the $\frac{\lambda}{B}$ separation at $10 \mu\text{m}$.

To generate a signal in the model four planetary parameters must be provided:

R	The planetary radius
T	The planets blackbody temperature
Sep	The angular separation between the host star and planet
PA	The position angle of the planet w.r.t. the vertical axis

A sketch displaying the definition of the position angle and separation is provided in Figure 8.

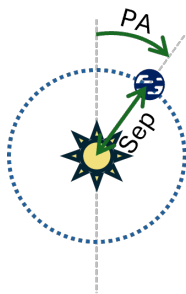


Fig. 8. Sketch of the observed planetary system viewed face-on, showing the definition of the separation and the position angle used. The drawing is not to scale.

2.6. Planet Reconstruction

To reconstruct the input parameters from the simulated noisy signal, the non-Linear least-squares Minimization and curve-FITting python library, (LMFIT; Newville et al. 2015), is used. The advantage of this library is that it simplifies the tracking of the parameters and easily incorporates setting parameter boundaries. Another benefit of employing LMFIT is the automatically generated fitting report which logs fitting data. After the fitting is completed LMFIT returns the estimated parameters based on the signal that was inputted, and a report. This report containing data such as the uncertainties and correlations associated with the found parameter values as well as general data on the performance of the fit.

For the single planet case an additional check was implemented with a MCMC (Markov Chain Monte Carlo) simulation to verify the convergence of the model. The MCMC simulation samples many values in order to estimate the posterior distribution of the estimated parameters. The Markov Chain especially

works to focus on regions of high likelihood (Diebolt & Robert 1994). In general it was found that the MCMC simulation results matched those from a single LMFIT-fitting closely and to save computational costs it was not re-implemented for the two planet case.

2.6.1. Single planet case

To reduce the scope of the investigation some boundaries are placed on the set of planetary systems being modeled. Firstly, due to the focus on temperate exoplanets, a planetary blackbody temperature of 300 K was assumed. Secondly, in a, face-on, single planet system the position angle only determines the starting point of the modulation sequence, and therefore does not need to be varied when observing only a single full rotation, like is done in this case. Finally, as was established in subsection 2.3, the sensitivity region of the full instrument starts at a separation of about 130 mas.

For the single planet case a MCMC simulation was implemented to ensure that the found parameters of a single fitting result were not merely coincidental. To visualize the found posterior distributions of the MCMC simulation a corner plot can be used which displays the relationship between the different parameters. In Figure 9 a simplified sketch of a corner plot is shown. The black outlined scatter plots each show a pair of parameters as a result of one iteration is plotted with respect to another. The shape created by the distribution of the points then illustrates correlation associated with this pair of parameters. In the sketch in Figure 9 a positive correlation between parameter A and B as can be observed by the oval outline bordering the distribution in the top left scatter plot. Contrarily parameters A and C are much less correlated, indicated by the circular shape of the cluster. On top of the parameter scatter plots, a corner plot displays the total distribution of the parameter using a histogram on the diagonal.

The performance of the configurations is evaluated based on the relative accuracy of the found mean value and the corresponding uncertainty compared with the original input value. The simulations are started in favorable conditions with the initial guessed value located at 5% above the true value. The simulation is performed for a variety of planet sizes to determine at which planet size the configurations are able to converge to the true value.

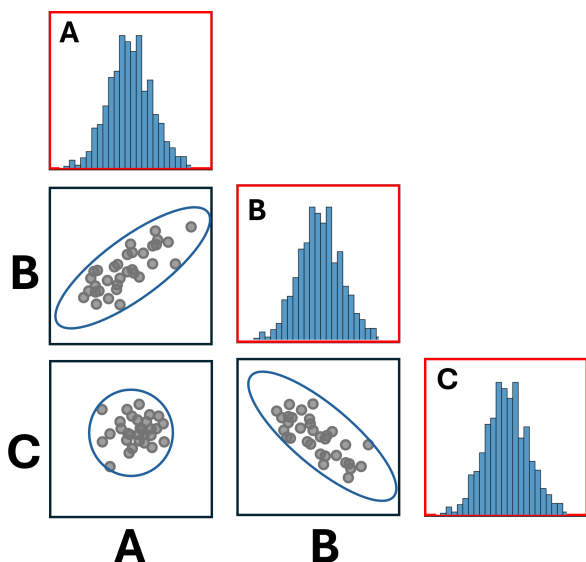


Fig. 9. Sketch showing the setup of a corner plot. In the black boxes the tested parameters, labeled A, B, and C, are plotted with respect to each other, the blue shapes contouring the distribution indicate the level of correlation between parameters. The red boxes show a histogram of the underlying distribution for the parameter in that column.

2.7. Modeling parameter correlations

The second category used to assess the performance of the configurations are the correlations between the parameters that follow from the fitting process. Some of these correlation can be explicitly traced, such as the use of a black body spectrum, described in Equation 6. Introducing a direct link between the radius and temperature of a modeled body. However, other correlations originate less obviously.

Spectral correlations in the model are introduced via phase differences between the beams. In the simulator these are inputted manually by the user by introducing a piston to the beam in the configuration file. In an actual instrument they could be the result of imperfections in the instrument such as chromatic aberrations, detector errors or due to the spectral binning. In the model they propagate into the results through the introduced optical path differences, they can be described using Equation 7

$$\Delta\phi = \frac{2\pi}{\lambda} \Delta s \quad (7)$$

Where $\Delta\phi$ is the introduced phase shift, λ is the wavelength and Δs is the optical path difference introduced due to the piston. Equation 7 shows the spectral relation of these OPDs. While the presence of correlations is not inherently problematic, it is relevant to evaluate how strong they are and how they may in turn influence the results.

To assess the correlations for the configurations a sampling approach is used. The on-sky view divided into pixels, a planet with a fixed radius and temperature is then generated and moved iteratively through the gridded map. The resulting fitting report is created for each planet location and the correlations per parameter pair are stored. A sketch of the approach is shown in Figure 10. To display the results a map is created for each parameter pair, where the color indicates the strength of the correlation for the given pair at each planet location. In other words, the squares

in the grid in Figure 10 are then colored for the strength of the correlation between the parameter pair.

To evaluate the performance of the configurations with respect to their correlations the behavior of the correlation for the different parameter pairs is compared. In general, lower correlation levels are favored. The correlation behavior is also compared with the uncertainties of each performed fitting to establish their impact on the fitting results.

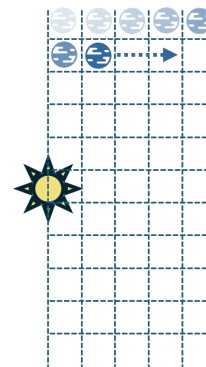


Fig. 10. Sketch of the correlation mapping approach. A planet with a fixed radius and temperature is sampled at each position in the grid. At each sampling the correlations between the parameters are recorded.

2.7.1. Two planet case

The final evaluated case is the performance of the systems in a two planet case. Adding another planet into the system leads to a superposition of the two signals. It therefore introduces a challenge to disentangle the contributions from both planets in the signal. The detection of planets in multi-planet systems is an ongoing challenge. A common strategy is to detect the planets sequentially. After a planet is detected it's signal is removed and the search is continued.

During this research the goal was not to solve this disentangling challenge. Instead the focus was placed on making a preliminary characterization of each configuration's behavior regarding the relative position of the two planets. No sequential approach was implemented, the planets were instead identified simultaneously by fitting the eight inputted planetary parameters, namely the temperatures, radii and positions. For this a case was tested where the inner planet was kept at a fixed location and a second planet sampled at a relative position angle from 0 to 180 deg, a sketch is provided in Figure 11.

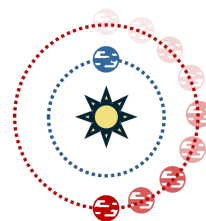


Fig. 11. Sketch of the modeled two planet system, the inner planet (blue) is kept fixed while the second planet (red) is sampled at different position angles between 0 and 180 degrees

To determine the performance of the planet fitting a similar comparison is performed as for the single planet case described in Section 2.6.1. The fitted parameter mean and uncertainty is

compared to the true value at each sampled relative position angle.

3. Results

Now that the model has been explained and the approach per evaluated case has been established, this section will continue with the results of the simulations. The results will be discussed per category, starting with the single planet case, in Section 3.1, and following this the assessment of the correlations, in Section 3.2, and the two planet case in Section 3.3.

3.1. Single planet performance

Like described in Section 2.6.1, the separation, position angle and temperature were kept constant and the size of the planet was used as the variable. The fitting was sampled in a MCMC-simulation. The performance of the configurations with respect to a varying planet size is displayed in Figure 12. The figure shows the four planetary parameters that were fitted each in an individual plot.

It can be observed that for the small planet sizes, between 1-2 R_e the fittings did not converge. Due to the correlated nature of the parameters in the model, if the fitting only successfully determined one parameter this does not mean that the fitting actually converged to the correct minimum. For example at 2.2 R_e the rectangular array seems to be spot-on in determining the radius, however its mean for the temperature was located at 670 K, over twice as hot as the input temperature. To preserve the information of the fitting performance for the correctly converged points the plots have been zoomed in, thereby cutting some of the failed convergence results.

For the defined planetary parameters it can be observed that the linear and kernel systems start to converge at planet sizes around 3 R_e . The rectangular array follows relatively quickly and reaches the true value around 4 R_e . The kernel nuller does show an occasional overestimation especially regarding the temperature/radius relation around 5 R_e .

The performance of the configurations is thus quite similar for the varying planet size scenarios. As mentioned in subsection 2.4, it is important to note that this research is focused on the relative performance and more advanced models are needed to set the true limits of the system. To verify the obtained results the same simulation was performed with the variable set to respectively the temperature and the separation. These showed similar performance results and they are included in Appendix A in Figures A.14 and A.15.

Like expected the performance of the systems generally improves when the planet size increases. Once the initial convergence is achieved the linear configuration seems to be most consistent across the tested scenarios. The rectangular array takes longer to converge to the correct scenario, after which its performance stays consistent as well.

Comparing the transmission maps of the linear configuration, in Figure 2 with those of the rectangular setup, in Figure 3, the linear pattern is only interrupted in one direction. This means that as long as the planet is located within the field of view it will show a fairly constant modulation signal in all spectral channels. In contrast, the rectangular array has more blind spots in the map, especially at higher wavelength channels, where the modulation may temporarily disappear in some spectral channels due to a gap in the pattern of the transmission map. Also reflected in the modulation efficiency at 130 mas shown in Figure 7. These drops

in sensitivity may explain why the rectangular array has slightly more trouble converging.

The kernel configuration also has gaps in the transmission map, however, due to the generation of three independent signals it is unlikely that the signal fully disappears. Compared to the double Bracewell setups, the splitting of the incoming signal leads to a lower signal amplitude in the individual modulations, shown in Figure 5. This might explain why the kernel configuration performs more inconsistently when determining the temperature and radius. These parameters are directly related to the flux, and thus amplitude, of the signal. In contrast, the kernel nuller performs much better in determining the position of the planet. The positioning in turn is linked to the intersection points of the modulation, for which it obtains more information compared to the linear and rectangular configurations.

To demonstrate the impact of correlations on the results and to visualize the distributions behind the points in Figure 12, a look can be taken at the corner plot shown in Figure 13. The results at each iteration of the MCMC-simulation are shown in the scatter plots. The correlations for each parameter pair are visible. It can be seen that for this case the kernel configuration is less correlated in terms of separation and temperature/radius, due to the more circular distribution of the points. The double Bracewell configurations show a respective positive correlation with temperature and a negative correlation with radius. Additionally, it can be observed that for the distributions involving the radius the distribution of the rectangular array is skewed and shows a non-Gaussian behavior. The expected strong correlation of radius and temperature is visible in the bottom right scatter plot where for all configurations the points are almost on a line.

3.2. Parameter Correlations

The second category assessed is the behavior of the correlations between the parameters. The correlations shown with the MCMC corner plot in Figure 13 are just for one specific case. To visualize the behavior in a broader context the correlations are mapped on a sky view. Which is achieved by moving a simulated planet through a gridded view of the on sky map, as discussed previously in Subsection 2.7. The resulting correlations for each parameter pair and configuration is shown in Figure 14.

The expected strong negative correlation between radius and temperature due to the blackbody model is immediately visible in the top right plot for each configuration. The correlations displayed in Figure 14 are determined with only a single iteration, due to the significant computational cost with the high number of points being assessed. Therefore, some pixelated regions can be found near the [0, 0] locations where the fitting failed to converge as a result of the low sensitivity of the instrument at these separation levels. The high sampling rate during the spacecraft rotation is shown in the centro-symmetric nature of the maps.

Comparing the two double Bracewell configurations some differences can be observed. Firstly, strong correlations are seen between the separation and flux (radius/temperature), in the left columns. The linear configuration shows a strong correlation in a relatively wide circle around the star, and reduces around the $\frac{\lambda}{b}$ at 10 μm separation to an opposite, lower correlation level. The rectangular array in turn shows a ringlike structure in the parameter correlations as the planet is moved away from the star. The strength of these correlations decreases at slightly lower separation compared to the linear setup just before the indicated $\frac{\lambda}{b}$ separation. Secondly, from the middle columns in Figure 14 it can be seen that position angle shows very little correlation for the double Bracewell setups, when zooming in only a faint spi-

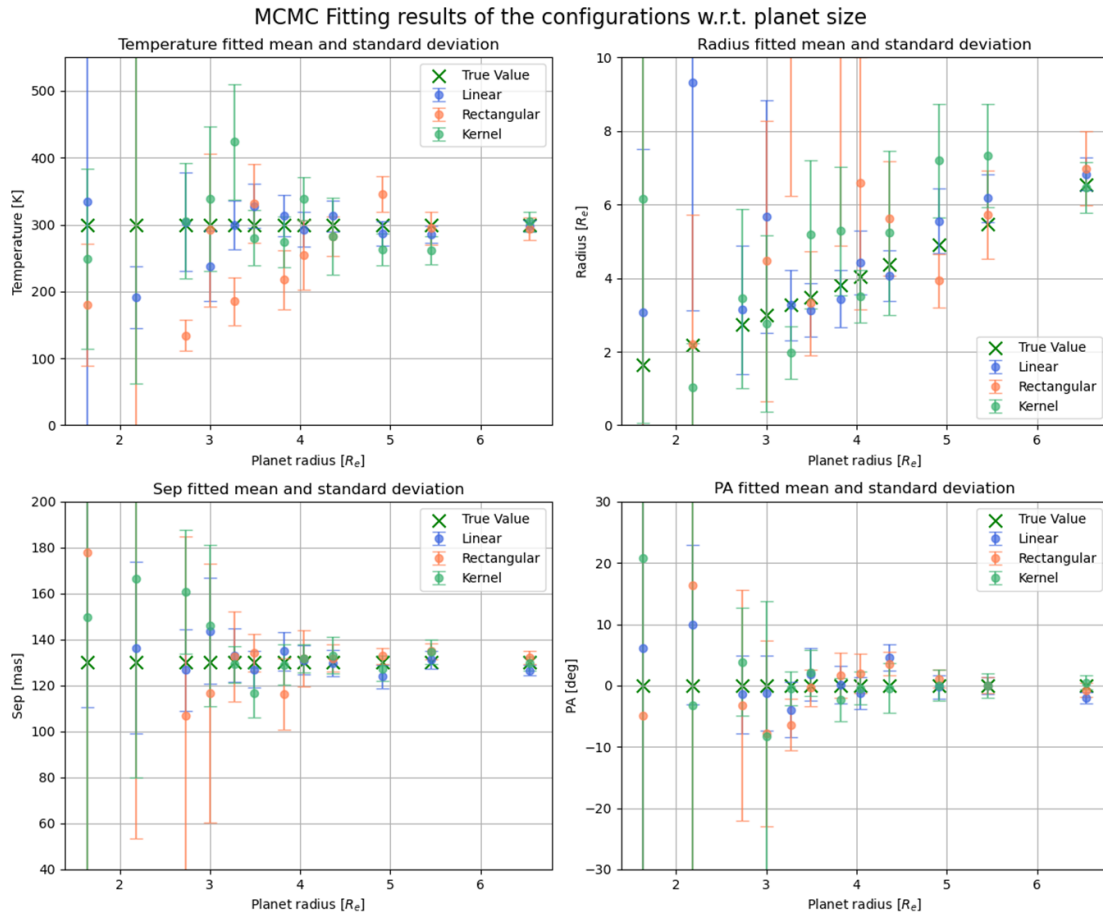


Fig. 12. MCMC-fitting results from the single planet modeled system with respect to a varying planet radius. The planet has a temperature of 300 K, a separation from the host star of 130 mas and is located at a position angle of 0 degrees. The different colors represent the different configuration, the inputted value is indicated in the plot by a green cross.

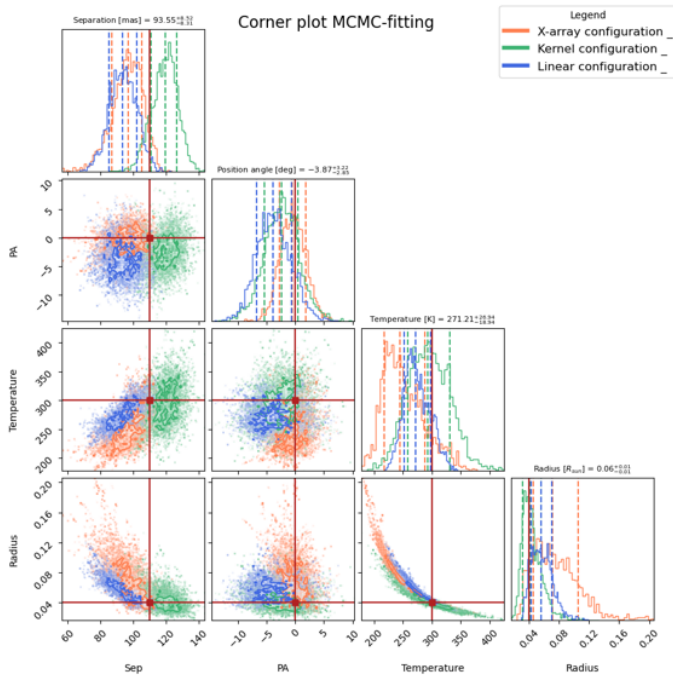


Fig. 13. Corner plot of MCMC fitting in a single planet case. The input is a planet with PA = 0 deg, separation = 110 mas, $R = 4.4 R_e$ $T = 300$ K. The red cross indicates the input value in the scatter plots.

ral pattern can be observed for both setups, the strength of the correlations remains < 0.25 .

The kernel configuration also shows relatively strong correlations between the parameters close to the star, within the low-sensitivity region. The separation shows a constant low correlation with the position angle in the top left plot for this setup. In contrast to the linear and rectangular setups, in the middle column correlations can also be observed with respect to the position angle at the lower separations.

Firstly, comparing the results of the correlations with respect to the separation, shown in the left columns of Figure 14. The linear and rectangular array configurations maintain relatively high correlation levels at greater separations compared to the kernel configuration. This higher correlation across the field of view for the double Bracewell configurations might be due to the single signal obtained at every spectral channel. The fitter is more prone to compensating errors in the fitting by adjusting another, given the limited data to constrain the fit. In contrast, the kernel design requires matching of three independent signals at each sampling point and channel, and compensating with the wrong parameter is more likely to introduce errors in the other signals, which likely reduces the extent of correlation observed.

The kernel configuration, however, shows strong correlations with respect to position angle, whereas these are negligible in the double Bracewell configurations. This lack of correlations in the double Bracewell nullers can likely be attributed to limitations in the modeling. It is assumed in the model that each

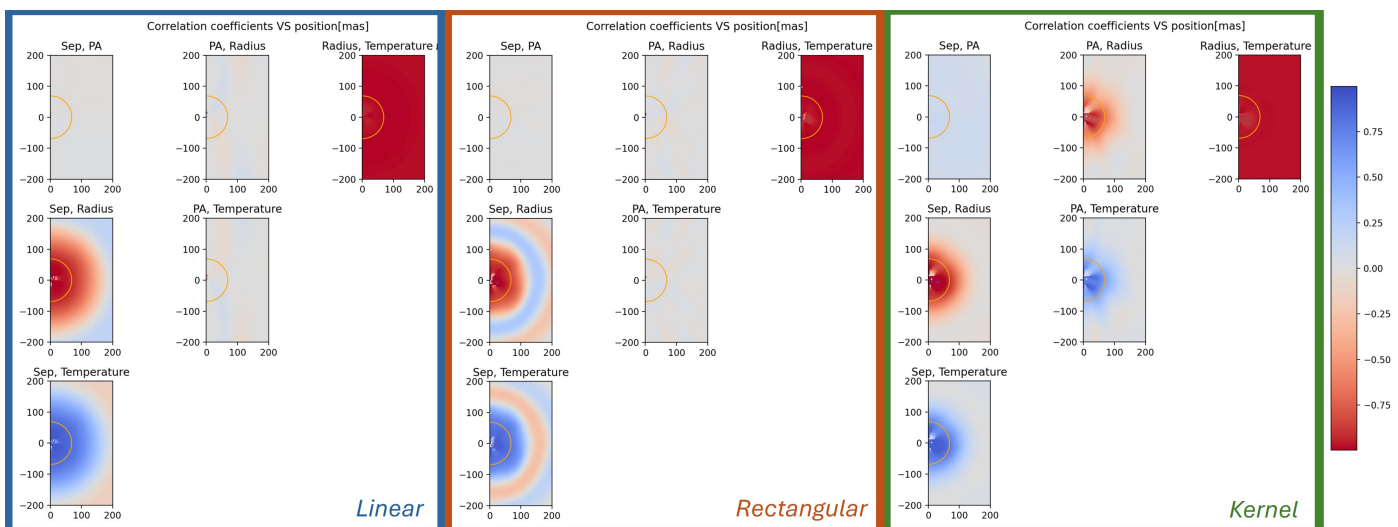


Fig. 14. Correlations between the parameters as function of the planet position for the three compared configurations. Each individual plot shows the correlation between one pair of parameters. The correlations are mapped on sky with the host star being located at $[0,0]$. Red shows a negative correlation and blue a positive one. The orange arch in the center displays the $\frac{\lambda}{B}$ value at $10 \mu\text{m}$.

sampled observation is independent, therefore temporal correlations in the signal are not modeled and the results in Figure 14 show only spectral correlations. The position angle is determined from the timing in the modulation and not from spectral effects like the other parameters. In the single output of the double Bracewell configurations the correlations associated with this parameter therefore likely do not show, even if they in reality might be present. The kernel configuration on the other hand has three independent signals at each timestamp and wavelength bin, and therefore these temporal correlations become visible.

To compare the impact of the correlations with the performance of the fit, the standard errors of the individual parameters sampled at the same time as the correlations can also be mapped, shown in Figure 15. It can be observed, as expected, that the highest uncertainties occur close to the star where the instrument is not fully sensitive. The linear configuration shows the lowest uncertainties across the field. The kernel configuration shows similar behavior, however more uncertainty can be observed regarding the radius and temperature compared to the linear setup. The rectangular array shows higher uncertainty levels, again especially for the radius and temperature. Here the ring like structure that was seen for the correlations also returns for these parameters.

3.3. Two planet system

The final evaluated category is the performance for a two planet system. The main relation evaluated here is to evaluate the ability of the configurations to fit the parameters with respect to the relative positions of the planets.

Before delving into the results of the full range of tested position angles a first brief look will be taken at the matched filter maps of a two planet system. In a matched filter a relatively weak signal is extracted from noisy data, this is done by assessing the correlation between the signal and a single planet (point) source. The color in the matched filter map, therefore shows the likelihood that the received signal originated from that location. It is not an image of the observed system. The data in these maps should therefore be treated somewhat carefully. However, they can be useful to help visualize some signal properties and to pro-

vide a starting point for fitting the planet locations. The matched filter maps for a two planet case with a difference in position angle of 115 degrees are displayed in Figure 16.

Each of the configurations has a distinct signature in the matched filter map as a result of the incoming signal. All three show a relatively bright coloring around the true planet locations indicating a sufficient signal to noise ratio to find the planets. The planetary signal creates an antisymmetric signature in the plot. This can lead to issues when one of the planets is located in the other's countersignature.

The linear configurations shows a blurred spread out signature between around the two planet locations and the found likelihoods in peak the highest for this configuration. The blurry nature of the map is thought to present problems when deconvoluting the planet signals (Lay 2005). The rectangular array in contrast has a almost checkered pattern around the center and more random noise can be seen due to the rougher surface in the plot. The second planet, located at the red cross, has a relatively low signature in the plot compared to the linear case. Finally the kernel shows the two planet locations most clearly, with two easily distinguishable yellow circles around the planet locations.

Now that a preliminary understanding of the signal behavior has been discussed, a look can be taken at the fitting performance for different relative positions. The setup of which was described in Section 2.7.1. An overview of the results is found in Figure 17. A set of eight plots is displayed. The two planets are separated by 50 mas, at 130 and 180 mas from the host star, the inner planet fitting is showed in the left four plots and the outer planet on the right.

Despite the differences in the matched filter maps in Figure 16 a decent fit is still obtained for all the configurations. Demonstrating that the matched filter maps should be used with care, even with the blurry nature of the map for the linear case the filter is still able to reconstruct the two planets.

The kernel configuration seems to struggle with the reconstruction when the planets are almost in line at relative position angles <25 , and quickly improves in performance after this. This behavior is observed for both the inner and outer planet. In a different tested scenario with the planets located further apart this

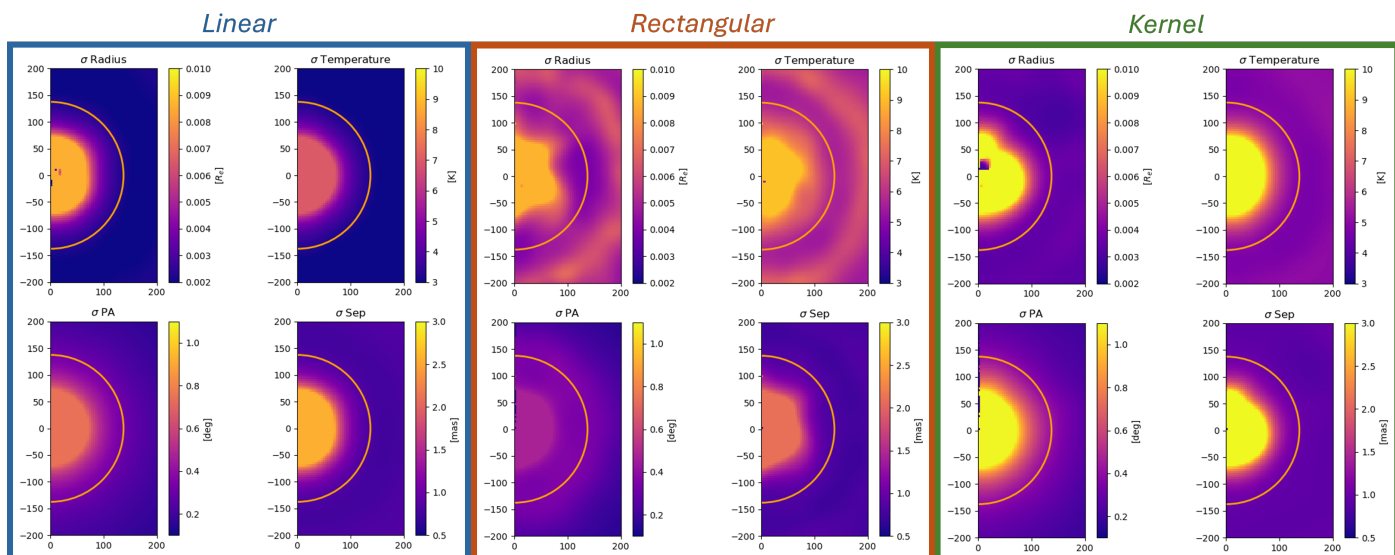


Fig. 15. Standard errors associated with the parameter fitting as a function of the planet position. The data the 10% highest data points are truncated to maintain the information outside the low-sensitivity region. The modeled planet has a radius of $5.5 R_e$ and a temperature of 300 K.

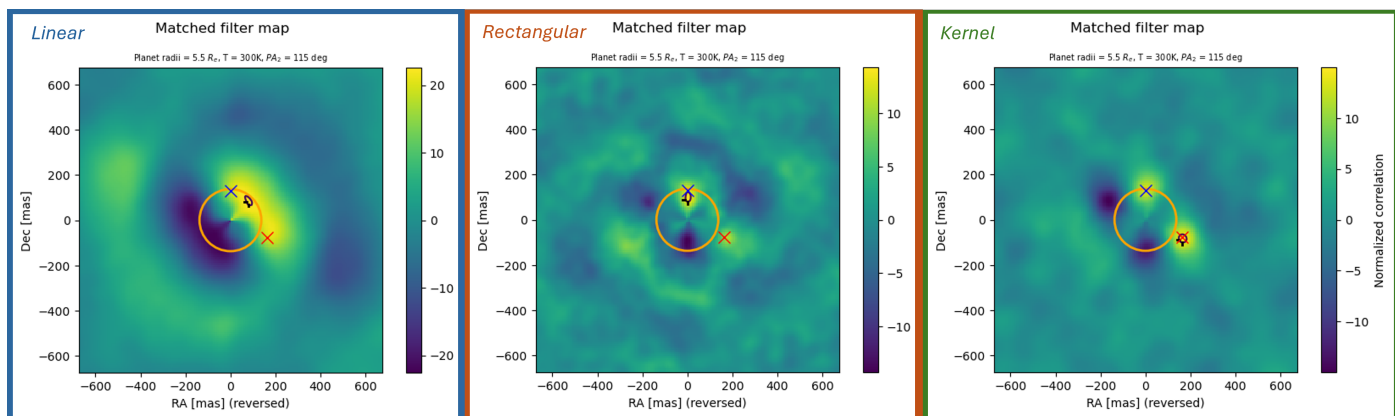


Fig. 16. Matched filter maps for the three configurations for a two planet case with planets at respectively sep = 130 mas and PA = 0 degrees (blue cross) and sep = 180 mas and PA = 115 degrees (red cross). The color shows the normalized correlation between the signal and the single point source. The orange circle indicates the $\frac{\lambda}{B}$ value at $10 \mu\text{m}$ and the contoured area shows the highest values in the plot.

behavior was not visible, the results of this iteration are included in the appendix in Figure A.18.

For the parameters of the outer planet the three configurations perform similarly. Looking at the inner planet the rectangular and kernel configurations follow a comparable pattern and are both very close to the correct values. Regarding the flux relation, the linear configuration seems to overestimate the size of the planet compared to its temperature, leading to a small offset compared to the other configurations.

It is however important to note that this fitting is based on a single iteration and only on one realization of the noise. It is recommended that a more thorough analysis is performed before being able to guarantee these trends in the observations.

4. Discussion

From these discussed results it is now possible to discuss the implications of some of the modeling choices made in this research.

4.1. Limitations of SCIFYsim

As highlighted in Section 2.4, SCIFYsim does not model the zodiacal effects or the temporal correlations. Exozodiacal dust in the habitable zone of stars has the same temperature as the modeled planets, approximately 300 K, and its effects will thus also be strongest in the highest SNR spectral channel at $10 \mu\text{m}$ Ertel et al. (2020). The symmetric contribution of the dust can be filtered by the the rotation of the array. However, the asymmetric structures will degrade the quality of the results.

Inclusion of temporal effects between the configurations will provide a more comprehensive overview of the noise present in the signal. This is particularly relevant for double Bracewell configurations, where each observation moment consists of a single data point, making these susceptible to temporal effects. Both of these limitations for SCIFYsim can be addressed with a more advanced simulator model such as the use of PHRINGE (PHotoelectron counts generatoR for nullING intErferometers), which is capable of modeling both zodiacal effects and temporal correlations to generate more accurate planetary signals (Huber et al. 2024).

Two planet fitting results w.r.t. PA - Planets at 130 and 180 mas

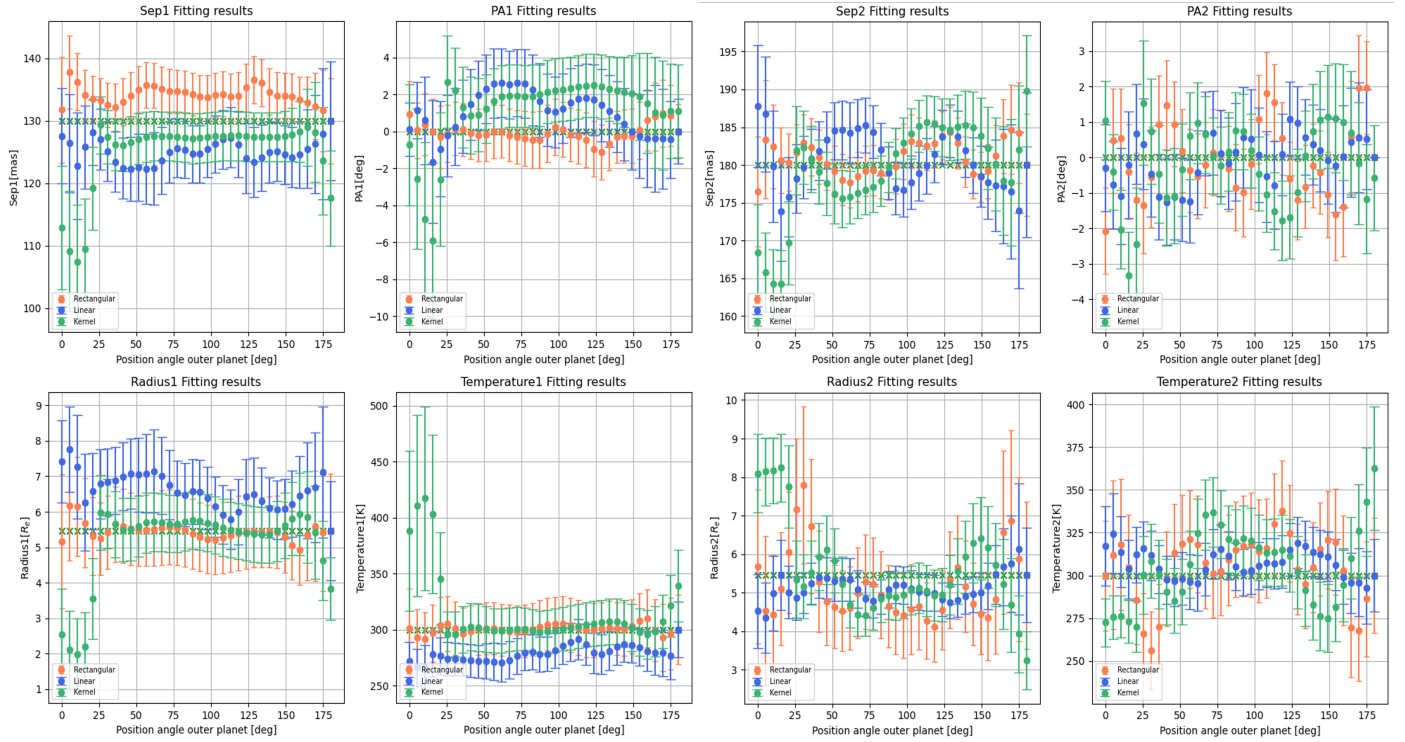


Fig. 17. Fitting results of the two planet fitting. The four plots on the left show the parameters of the inner planet and on the right the fitting of the outer planet is shown. The dots show the fitted mean and the error bars indicate the standard error. The colors in the plot are linked to the different configurations

Previous simulation performed in support of LIFE mostly employed LIFESim, which does incorporate zodiacal effects, however in turn neglects instrumental noise. At the start of this thesis no simulation tools existed that were developed sufficiently to incorporate both these effects. It is expected that a more thorough analysis of the noise affecting the systems an absolute evaluation of the performance can be achieved in complement to the relative analysis in this research.

4.2. MCMC implementation in the two planet case

Due to the limited computational capacity a MCMC-simulation was not implemented for the evaluated two planet case. A comparison between single-iteration results and MCMC-derived parameters in the single-planet case showed close agreement when the SNR was high, indicating that a single iteration can provide reliable estimates in these favorable conditions.

In this study, the two planet system was modeled with relatively large planets, of $5.5 R_e$, which could be constrained effectively by the model. However, if the analysis was expanded to smaller planets, closer to the system's performance limit a single fitting approach may no longer be sufficient. In these cases a more advanced simulation is needed to ensure a robust estimation of the parameters. The implementation of the MCMC simulation for a multi planet case could solidify the trends observed in Figure 17.

4.3. Scope of the multi-planet systems

The dimensionality of the planet fitting expands rapidly with the inclusion of additional planets. In this work only a limited as-

essment was performed to test the performance in a multi planet case. Future work should aim to expand the scope of the parameter space that is evaluated. Both in terms of a two planet case by incorporating variations of the separations and planet types and by expansion to systems with more planets.

In this research a good fitting could be achieved for two planets with a relatively simple fitting method. Going to more complex systems a more advanced strategy may be recommended. For example by the employment of sequential fitting of the planets or by use of a Fourier analysis to disentangle the various planet's frequency contributions, or the implementation of machine learning algorithms in even more complex cases.

4.4. Overall performance

Comparing the performance of the different configurations across all categories there does not seem to be a clear winner that excelled in performance each time. Comparing the two double Bracewell nullers the linear design shows a slight advantage terms of the single planet fitting. The relatively simple transmission map and therefore sine-like modulation pattern seems to be more easily retrieved by the fitter. There are no gaps in the transmission map so the sensitivity within the field of view is very consistent across the spectral channels. However, when expanding to a two planet system this advantage seems to disappear somewhat.

The kernel setup shows a lot of promise for multiplanet systems. The three independent signals lead to a great ability to locate the planets as was shown in the single planet fitting and also in the matched filter map for a two planet case. The splitting of the signal does however seem to lead to more uncertainty

when determining the flux of the signal and therefore with fitting the correct temperature and radius. It might be that a higher throughput of the instrument with more signal photons reaching the detector this drawback may be compensated. The kernel configuration also shows fewer correlations between the fitted parameters.

The rectangular array performed slightly worse for the single planet case. However, in the fitting of the two planet systems it performed better in the tested case than the linear array. A more robust analysis of the multi planet systems is needed to see if this holds true.

5. Conclusion

In this research a comparison was made between three possible configurations for a single spacecraft nulling interferometry precursor mission aiming to detect and characterize exoplanets. The comparison was performed using an instrument simulator and their performance was assessed based on three categories, (1) their ability to constrain planetary parameters in a single planet system, (2) the behavior of the correlations between the parameters in the fitting process and (3) their ability to fit a two planet system.

5.1. Single planet case

For the single planet case, the size of the planet was made a variable and the temperate planet was placed at a separation of 130 mas, where the instrument is sensitive to most observed wavelengths. It was found that the linear array converged to the correct planetary parameters the quickest at about $3 R_e$. Followed quickly by the kernel and then the rectangular double Bracewell. The performances were relatively similar. It is likely the relatively simple modulation scheme associated with the linear array geometry and the full coverage of the transmission pattern, which make this configuration the most consistent in this test case.

The kernel array also especially showed similar performance in terms of finding the planet position, however it performed worse when fitting the temperature and radius of the simulated planet.

5.2. Correlation behavior

In terms of correlations the configurations show distinct behavior with relation to the position of the planet. It was found that below the $\frac{\lambda}{B}$ at $10 \mu\text{m}$ separation the correlations are significantly higher than outside this region. The kernel configuration showed the lowest correlation levels outside this central region. The double Bracewell configurations showed almost no correlation with respect to position angle in this simulation, however this is likely attributed to the exclusion of temporal effects in the simulator.

5.3. Two planet case

For the two planet case the superposition of the two planet signals lead to a convolution of both signals, which can lead to signals canceling each other out. This may occur especially for nearby planets and planets opposing each other. In the fitting of two planet systems the kernel and the rectangular array were most successful in constraining the planet parameters, however the linear array is not far off, it mostly showed a slight offset for the fitting of the inner planet. In the tested scenario the kernel

configuration shows some trouble especially when the planets are in an in line position. The matched filter map shows great promise for the kernel configurations in locating different planets.

5.4. Recommendations

Overall there is not a single clear winner from the performed comparison. Each configuration has certain advantages and disadvantages that may lead to it being the best fit for a potential mission. This study also neglects many design components, such as mechanical and optical design constraints that could lead to a potential favor for a given configuration.

Nevertheless from this analysis it seems that the linear configuration performs most consistently when retrieving the parameters of a single planet system. The kernel configuration shows the most potential in terms of constraining multi planet systems, due to its reduced correlations in the field and ability to isolate planet positions. However, with the assumptions on efficiencies and errors used in this research, the splitting of the signal does lead to potential issues in terms of fitting the flux of the planet. The rectangular array showed a similar performance to the kernel in the tested two planet scenario.

It is recommended that a more advanced approach for fitting multi-planet systems is employed in combination with a more complete exploration of the variables involved in order to make a more complete statement about their performance with multi planet systems.

References

- Angel, J. & Woolf, N. 1997, *The astrophysical journal*, 475, 373
- Beichman, C., Lawson, P., Lay, O., et al. 2006, in *Advances in Stellar Interferometry*, Vol. 6268, SPIE, 245–253
- Bracewell, R. N. 1978, *Nature*, 274, 780
- Dandumont, C., Defrère, D., Kammerer, J., et al. 2020, *Journal of Astronomical Telescopes, Instruments, and Systems*, 6, 035004
- Dannert, F. A., Ottiger, M., Quanz, S. P., et al. 2022, *Astronomy & Astrophysics*, 664, A22
- Defrère, D., Absil, O., Den Hartog, R., Hanot, C., & Stark, C. 2010, *A&A*, 509, A9
- Diebolt, J. & Robert, C. P. 1994, *Journal of the Royal Statistical Society: Series B (Methodological)*, 56, 363
- Ertel, S., Defrère, D., Hinz, P., et al. 2020, *The Astronomical Journal*, 159, 177
- Glauser, A. M., Quanz, S. P., Hansen, J., et al. 2024, in *Optical and Infrared Interferometry and Imaging IX*, Vol. 13095, SPIE, 354–374
- Guyon, O., Mennesson, B., Serabyn, E., & Martin, S. 2013, *Publications of the Astronomical Society of the Pacific*, 125, 951
- Huber, P. A., Dannert, F. A., Laugier, R., et al. 2024, in *Optical and Infrared Interferometry and Imaging IX*, Vol. 13095, SPIE, 382–391
- Laugier, R., Cvetojevic, N., & Martinache, F. 2020, *Astronomy & Astrophysics*, 642, A202
- Laugier, R., Defrère, D., & Bigioli, A. 2021, in *SF2A-2021: Proceedings of the Annual meeting of the French Society of Astronomy and Astrophysics*, 339–342
- Lawson, P., Lay, O., Martin, S., et al. 2008, in *Optical and Infrared Interferometry*, Vol. 7013, SPIE, 858–872
- Lay, O. P. 2004, *Applied Optics*, 43, 6100
- Lay, O. P. 2005, *Applied Optics*, 44, 5859
- Lay, O. P. 2006, in *Advances in Stellar Interferometry*, Vol. 6268, SPIE, 404–416
- Lay, O. P. & Dubovitsky, S. 2004, in *New Frontiers in Stellar Interferometry*, Vol. 5491, SPIE, 874–885
- Leger, A. & Herbst, T. 2007, arXiv preprint arXiv:0707.3385
- Loicq, J., Defrère, D., Laugier, R., et al. 2024, in *Optical and Infrared Interferometry and Imaging IX*, Vol. 13095, SPIE, 812–822
- Martinache, F. & Ireland, M. J. 2018, *Astronomy & Astrophysics*, 619, A87
- Newville, M., Stensitzki, T., Allen, D. B., & Ingarola, A. 2015, *LMFIT: Non-Linear Least-Square Minimization and Curve-Fitting for Python*
- Ollivier, M. & Mariotti, J.-M. 1997, *Applied Optics*, 36, 5340
- Quanz, S. P., Ottiger, M., Fontanet, E., et al. 2022, *Astronomy & Astrophysics*, 664, A21
- Tacconi, L. J., Arridge, C. S., & Buonanno, A. 2021, *Voyage 2050 Final recommendations from the Voyage 2050 Senior Committee*
- Zoubir, A. M. & Iskander, D. R. 2007, *IEEE Signal Processing Magazine*, 24, 10

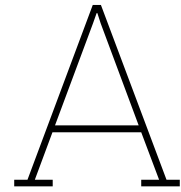
Part III

Appendices

References

- [1] Olivier Absil, Anders Karlsson, and Lisa Kaltenecker. “Inherent modulation: a fast chopping method for nulling interferometry”. In: *Interferometry in Space*. Vol. 4852. SPIE. 2003, pp. 431–442.
- [2] JRP Angel and NJ Woolf. “An imaging nulling interferometer to study extrasolar planets”. In: *The astrophysical journal* 475.1 (1997), p. 373.
- [3] Charles Beichman et al. “Status of the terrestrial planet finder interferometer (TPF-I)”. In: *Advances in Stellar Interferometry*. Vol. 6268. SPIE. 2006, pp. 245–253.
- [4] *Beugung und Interferenz am Doppelspalt*. 2013. URL: <https://www.cobocards.com/pool/de/card/7puji0113/online-karteikarten-beugung-und-interferenz-am-doppelspalt/>.
- [5] Ronald N Bracewell. “Detecting nonsolar planets by spinning infrared interferometer”. In: *Nature* 274.5673 (1978), pp. 780–781.
- [6] Colin Dandumont et al. “Exoplanet detection yield of a space-based Bracewell interferometer from small to medium satellites”. In: *Journal of Astronomical Telescopes, Instruments, and Systems* 6.3 (2020), pp. 035004–035004.
- [7] Colin Dandumont et al. “Performance study of interferometric small-sats to detect exoplanets: updated exoplanet yield and application to nearby exoplanets”. In: *Optical and Infrared Interferometry and Imaging VII*. Vol. 11446. SPIE. 2020, pp. 557–570.
- [8] Felix A Dannert et al. “Large interferometer for exoplanets (life)-ii. signal simulation, signal extraction, and fundamental exoplanet parameters from single-epoch observations”. In: *Astronomy & Astrophysics* 664 (2022), A22.
- [9] Denis Defrère et al. “L-band nulling interferometry at the VLTI with Asgard/NOTT: status and plans”. In: *Optical and Infrared Interferometry and Imaging IX*. Vol. 13095. SPIE. 2024, pp. 92–102.
- [10] Defrère, D. et al. “Nulling interferometry: impact of exozodiacal clouds on the performance of future life-finding space missions*”. In: *A&A* 509 (2010), A9. DOI: 10.1051/0004-6361/200912973. URL: <https://doi.org/10.1051/0004-6361/200912973>.
- [11] David J Des Marais et al. “Remote sensing of planetary properties and biosignatures on extrasolar terrestrial planets”. In: *Astrobiology* 2.2 (2002), pp. 153–181.
- [12] Steve Ertel et al. “The HOSTS survey for exozodiacal dust: observational results from the complete survey”. In: *The Astronomical Journal* 159.4 (2020), p. 177.
- [13] DJ Fixsen and Eli Dwek. “The zodiacal emission spectrum as determined by COBE and its implications”. In: *The Astrophysical Journal* 578.2 (2002), p. 1009.
- [14] Adrian M Glauser et al. “The Large Interferometer For Exoplanets (LIFE): a space mission for mid-infrared nulling interferometry”. In: *Optical and Infrared Interferometry and Imaging IX*. Vol. 13095. SPIE. 2024, pp. 354–374.
- [15] Olivier Guyon et al. “Optimal beam combiner design for nulling interferometers”. In: *Publications of the Astronomical Society of the Pacific* 125.930 (2013), p. 951.
- [16] Jonah T Hansen and Michael J Ireland. “Large Interferometer For Exoplanets (LIFE)-IV. Ideal kernel-nulling array architectures for a space-based mid-infrared nulling interferometer”. In: *Astronomy & Astrophysics* 664 (2022), A52.
- [17] E. Hecht. *Optics*. 5th ed. Harlow, England: Pearson Education Limited, 2017.
- [18] S Jacquinod et al. “PERSEE: a nulling interferometer with dynamic correction of external perturbations”. In: *International Conference on Space Optics—ICSO 2008*. Vol. 10566. SPIE. 2017, pp. 219–226.

- [19] T Kelsall et al. “The COBE diffuse infrared background experiment search for the cosmic infrared background. II. Model of the interplanetary dust cloud”. In: *The Astrophysical Journal* 508.1 (1998), p. 44.
- [20] Romain Laugier, Nick Cvetojevic, and Frantz Martinache. “Kernel nullers for an arbitrary number of apertures”. In: *Astronomy & Astrophysics* 642 (2020), A202.
- [21] Romain Laugier et al. “Asgard/nott: L-band nulling interferometry at the vlt-i. simulating the expected high-contrast performance”. In: *Astronomy & Astrophysics* 671 (2023), A110.
- [22] PR Lawson et al. “Terrestrial planet finder interferometer: 2007-2008 progress and plans”. In: *Optical and Infrared Interferometry*. Vol. 7013. SPIE. 2008, pp. 858–872.
- [23] Oliver P Lay. “Systematic errors in nulling interferometers”. In: *Applied Optics* 43.33 (2004), pp. 6100–6123.
- [24] J-M Le Duigou et al. “PEGASE: a free flying interferometer for the spectroscopy of giant exoplanets”. In: *International Conference on Space Optics—ICSO 2006*. Vol. 10567. SPIE. 2017, pp. 9–18.
- [25] Jean-Michel Le Duigou et al. “Pegase: a space-based nulling interferometer”. In: *Space Telescopes and Instrumentation I: Optical, Infrared, and Millimeter*. Vol. 6265. SPIE. 2006, pp. 495–508.
- [26] Alain Leger and Tom Herbst. “DARWIN mission proposal to ESA”. In: *arXiv preprint arXiv:0707.3385* (2007).
- [27] Jérôme Loicq et al. “Single spacecraft nulling interferometer for exoplanets: preliminary concept”. In: *Optical and Infrared Interferometry and Imaging IX*. Vol. 13095. SPIE. 2024, pp. 812–822.
- [28] Frantz Martinache and Michael J Ireland. “Kernel-nulling for a robust direct interferometric detection of extrasolar planets”. In: *Astronomy & Astrophysics* 619 (2018), A87.
- [29] Matt Newville and Renee Otten et al. *Imfit/Imfit-py: 1.3.2*. Version 1.3.2. July 2024. DOI: 10.5281/zenodo.12785036. URL: <https://doi.org/10.5281/zenodo.12785036>.
- [30] M Ollivier et al. “PEGASE, an infrared interferometer to study stellar environments and low mass companions around nearby stars”. In: *Experimental Astronomy* 23 (2009), pp. 403–434.
- [31] Sascha P Quanz et al. “Atmospheric characterization of terrestrial exoplanets in the mid-infrared: biosignatures, habitability, and diversity”. In: *Experimental astronomy* (2021), pp. 1–25.
- [32] Sascha Patrick Quanz et al. “Large Interferometer For Exoplanets (LIFE)-I. Improved exoplanet detection yield estimates for a large mid-infrared space-interferometer mission”. In: *Astronomy & Astrophysics* 664 (2022), A21.
- [33] Daniel Rouan. “Nulling Interferometry”. In: *Encyclopedia of Astrobiology*. Ed. by Muriel Gargaud et al. Berlin, Heidelberg: Springer Berlin Heidelberg, 2011, pp. 1152–1155. ISBN: 978-3-642-11274-4. DOI: 10.1007/978-3-642-11274-4_1088. URL: https://doi.org/10.1007/978-3-642-11274-4_1088.
- [34] Chandrasekhar Roychoudhuri and Kevin R Lefebvre. “Van Cittert-Zernike theorem for introductory optics course using the concept of fringe visibility”. In: *1995 International Conference on Education in Optics*. Vol. 2525. SPIE. 1995, pp. 148–160.
- [35] Eugene Serabyn et al. “Nulling at short wavelengths: theoretical performance constraints and a demonstration of faint companion detection inside the diffraction limit with a rotating-baseline interferometer”. In: *Monthly Notices of the Royal Astronomical Society* 489.1 (2019), pp. 1291–1303.
- [36] Linda J. Tacconi, Christopher S. Arridge, and Alessandra Buonanno. *Voyage 2050 Final recommendations from the Voyage 2050 Senior Committee*. May 2021. URL: <https://www.cosmos.esa.int/web/voyage-2050/home>.
- [37] Eric Thiébaud and Laurent Mugnier. “Maximum a posteriori planet detection and characterization with a nulling interferometer”. In: *Proceedings of the International Astronomical Union* 1.C200 (2005), pp. 547–552. ISSN: 17439221. DOI: 10.1017/S1743921306009938.
- [38] Aleksander Wolszczan and Dail A Frail. “A planetary system around the millisecond pulsar PSR1257+12”. In: *Nature* 355.6356 (1992), pp. 145–147.



Additional Figures

This appendix shows a number of additional figures that were created over the course of the research. section A.1 provides an overview of all configuration specific figures that summarize the instrument response. section A.2 shows additional results that were obtained and used either in the process of obtaining the final results or support the discussed findings.

A.1. Configuration specific figures

Below follow the figures displaying the figure responses of respectively the linear double Bracewell, in subsection A.1.1, the rectangular double Bracewell, in subsection A.1.2 and finally the kernel in subsection A.1.3.

A.1.1. Linear double Bracewell configuration

The response of the system is visualized using the transmission maps and corresponding modulations, these are presented below.

Transmission maps

Below the transmission maps of the linear double Bracewell are displayed Figure A.1 shows the raw transmission maps of the two extreme wavelength bins that follow from the 4 outputs after the combiner. The differential transmission map, resulting from the pairwise combination of (dark) output 1 and output 2 is shown in Figure A.2.

Modulations and efficiencies

Below are some supporting figures to show the modulation behavior that follows from the differential transmission map displayed in Figure A.2. Firstly Figure A.3 shows the modulation across the spectral channels for a planet located at $[0, 100]$. Following this Figure A.4 displays the corresponding modulation efficiencies.

A.1.2. Rectangular double Bracewell configuration

Below the transmission maps and modulation efficiencies of the rectangular double Bracewell configuration are shown. The two dimensional nature of the array also leads to an additional dimension in the fringe spacing.

Transmission maps

Firstly, the transmission maps of the rectangular double Bracewell. The raw transmission maps of the two extreme wavelength bins that follow from the 4 outputs after the combiner are shown in Figure A.5. The differential transmission map, resulting from the pairwise combination of (dark) output 1 and output 2 is shown in Figure A.6.

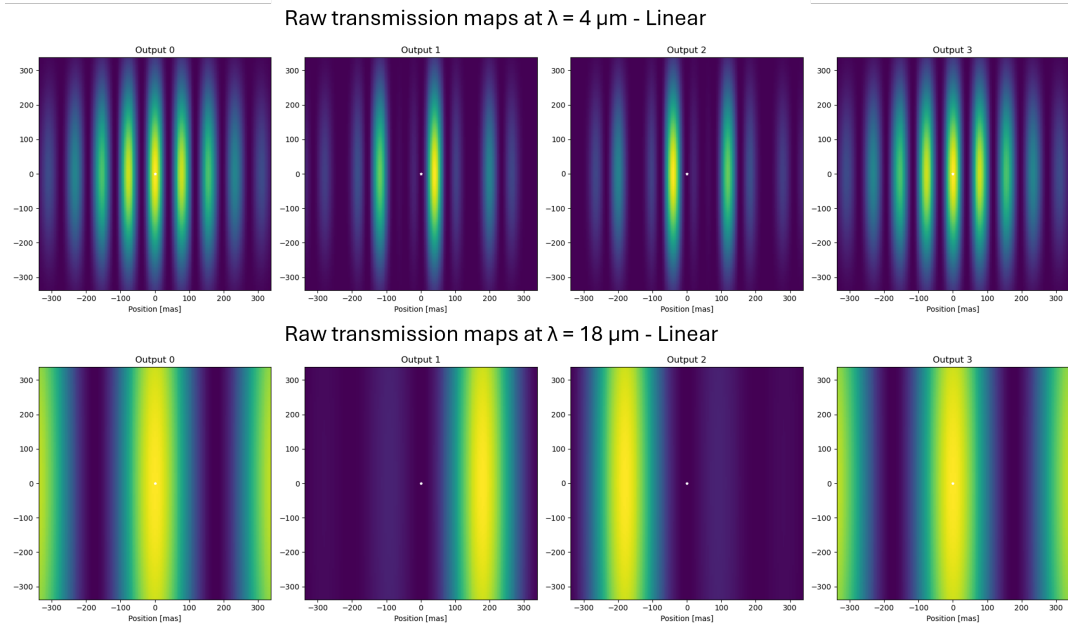


Figure A.1: Transmission maps resulting from the beam combination in the linear double Bracewell nullo. Output 0 and 3 show the bright outputs and output 1 and 2 the dark outputs. The top row are the shortest wavelength bin at $4 \mu\text{m}$ and the bottom row the longest wavelength at $18 \mu\text{m}$.

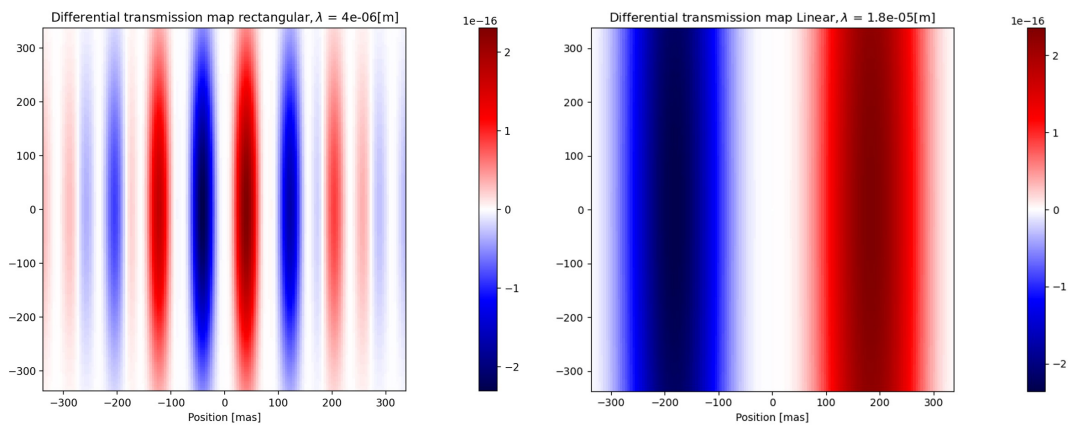


Figure A.2: Differential transmission map of the linear double Bracewell configuration at respectively $4 \mu\text{m}$ and $18 \mu\text{m}$.

— Modulations between 4-18 μm for a planet at [0,100] —

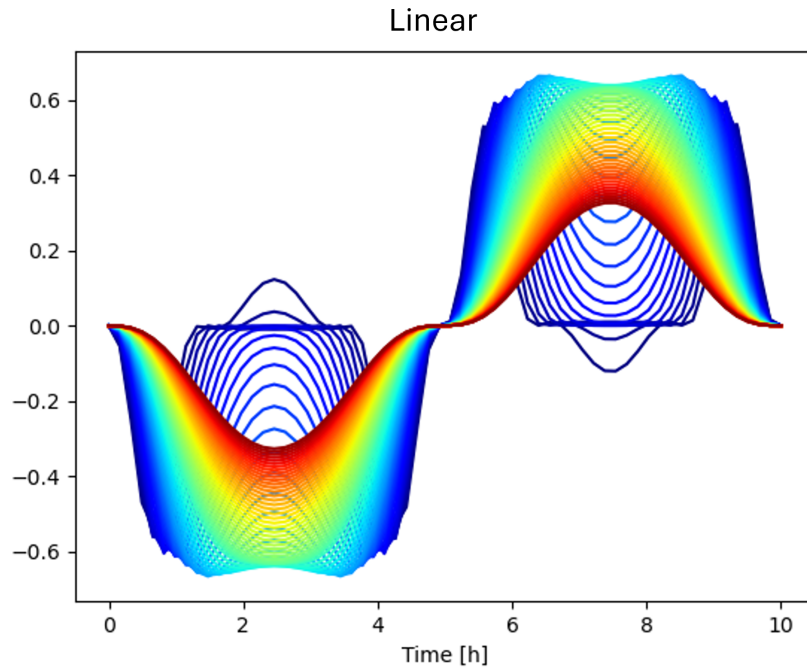


Figure A.3: Signal modulations for the linear configuration, for a planet located at [0, 100] in case of no noise.

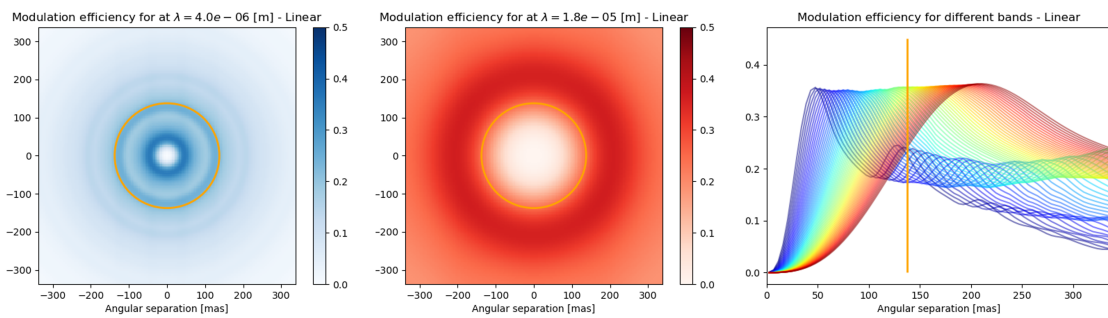


Figure A.4: Modulation efficiencies for the rectangular configuration. The left two plots show the modulation efficiencies for spectral channel 4 μm and 18 μm in the observed field. the righter most plot shows the development of the modulation efficiencies as a function of separation for all wavelengths. The orange indicator shows the $\frac{\lambda}{B}$ separation at 10 μm .

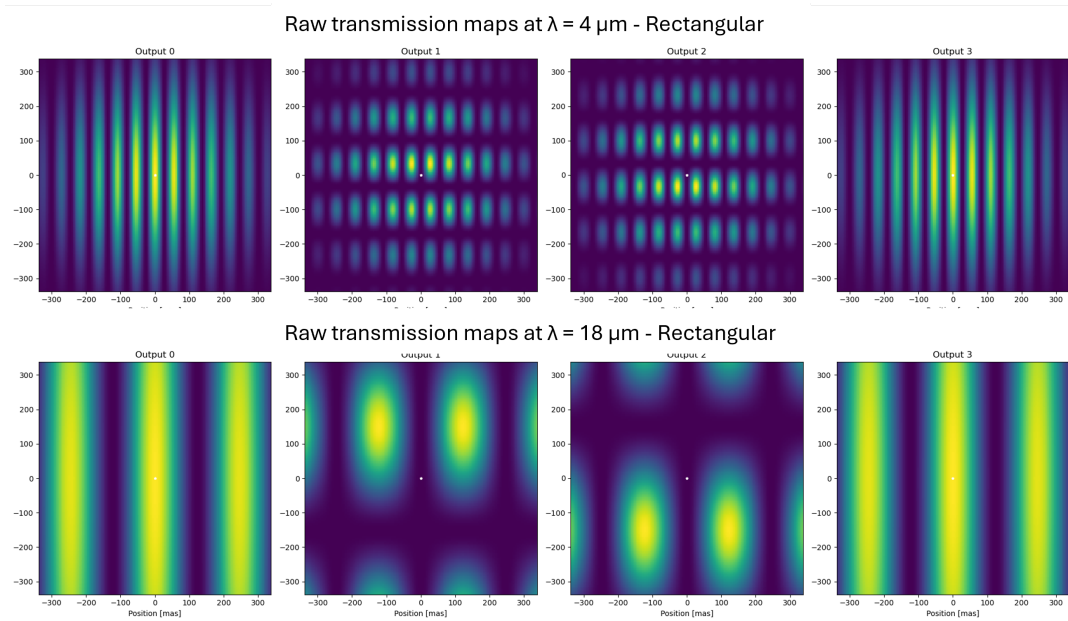


Figure A.5: Transmission maps resulting from the beam combination in the rectangular double Bracewell nuller. Output 0 and 3 show the bright outputs and output 1 and 2 the dark outputs. The top row are the shortest wavelength bin at $4 \mu\text{m}$ and the bottom row the longest wavelength at $18 \mu\text{m}$.

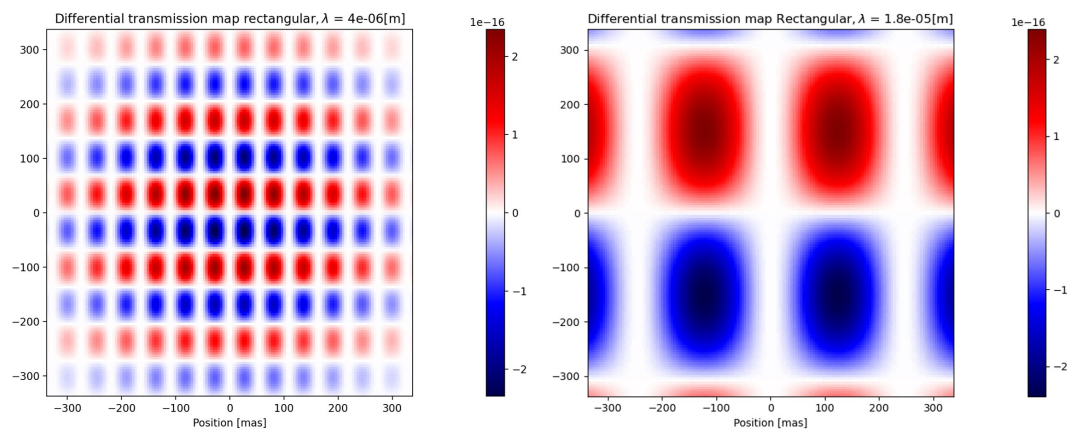


Figure A.6: Differential transmission map of the rectangular double Bracewell configuration at respectively $4 \mu\text{m}$ and $18 \mu\text{m}$.

Modulations and efficiencies

Secondly, the corresponding modulation response of the rectangular double Bracewell is shown in Figure A.7. The resulting modulation efficiencies are summarized in Figure A.8.

Modulations between 4-18 μm for a planet at [0,100]

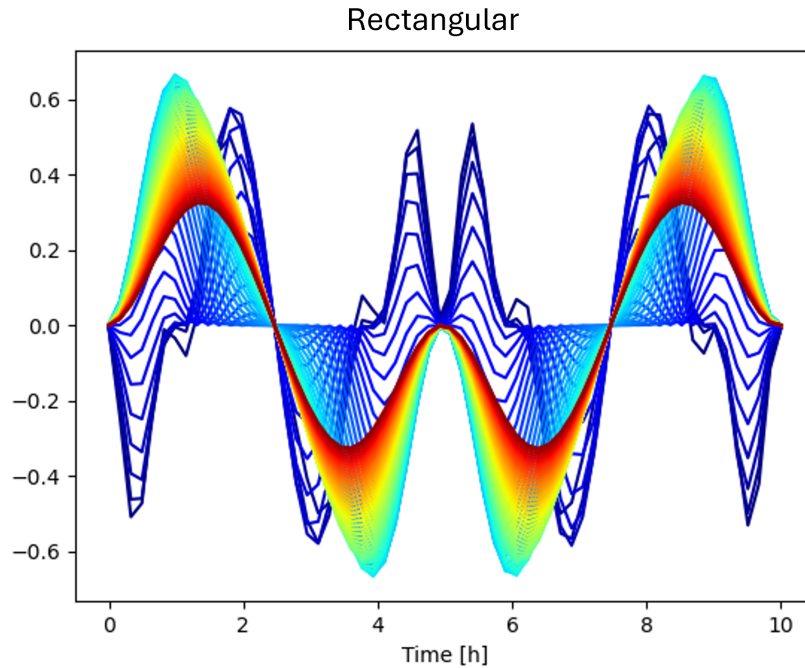


Figure A.7: Signal modulations for the rectangular configuration, following from the differential transmission map for a simulated planet at [0, 100] in a no noise case.

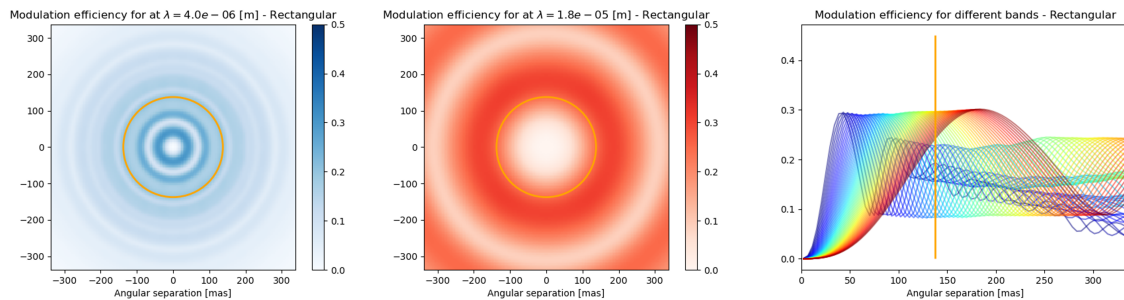


Figure A.8: Modulation efficiencies for the rectangular configuration. The left two plots show the modulation efficiencies for spectral channel 4 μm and 18 μm in the observed field. the righter most plot shows the development of the modulation efficiencies as a function of separation for all wavelengths. The orange indicator shows the $\frac{\lambda}{B}$ separation at 10 μm

A.1.3. Kernel four telescope configuration

Finally the response of the kernel nuller is summarized with the transmission maps and efficiencies presented below. In contrast to the double Bracewell configurations the kernel has six raw outputs and in turn three differential outputs.

Transmission maps

The raw outputs after the 4x7 combination are shown in Figure A.9. The recombined differential maps are shown in Figure A.10.

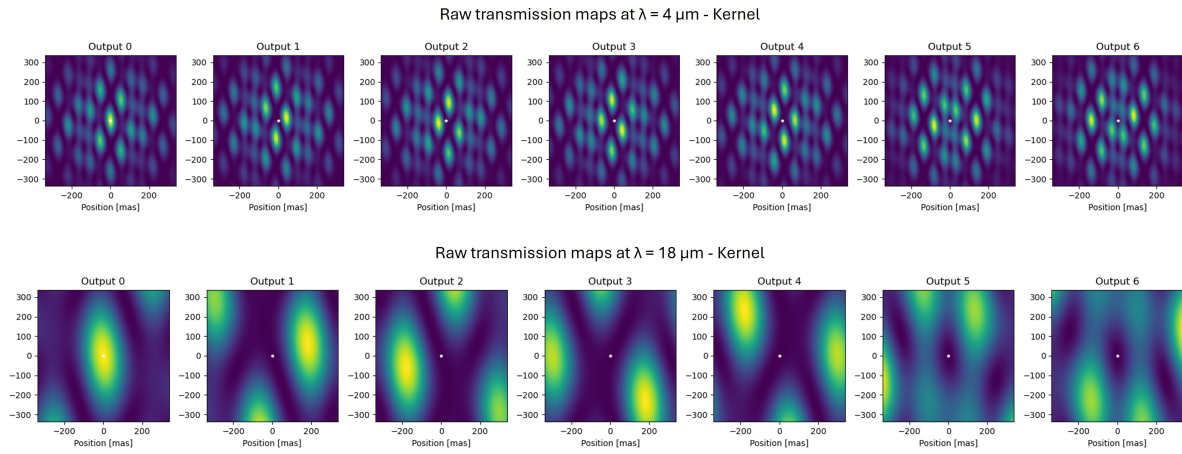


Figure A.9: Transmission maps resulting from the beam combination in the kernel nuller. Output 0 shows the bright outputs and the others the dark outputs. The top row are the shortest wavelength bin at $4 \mu\text{m}$ and the bottom row the longest wavelength at $18 \mu\text{m}$.

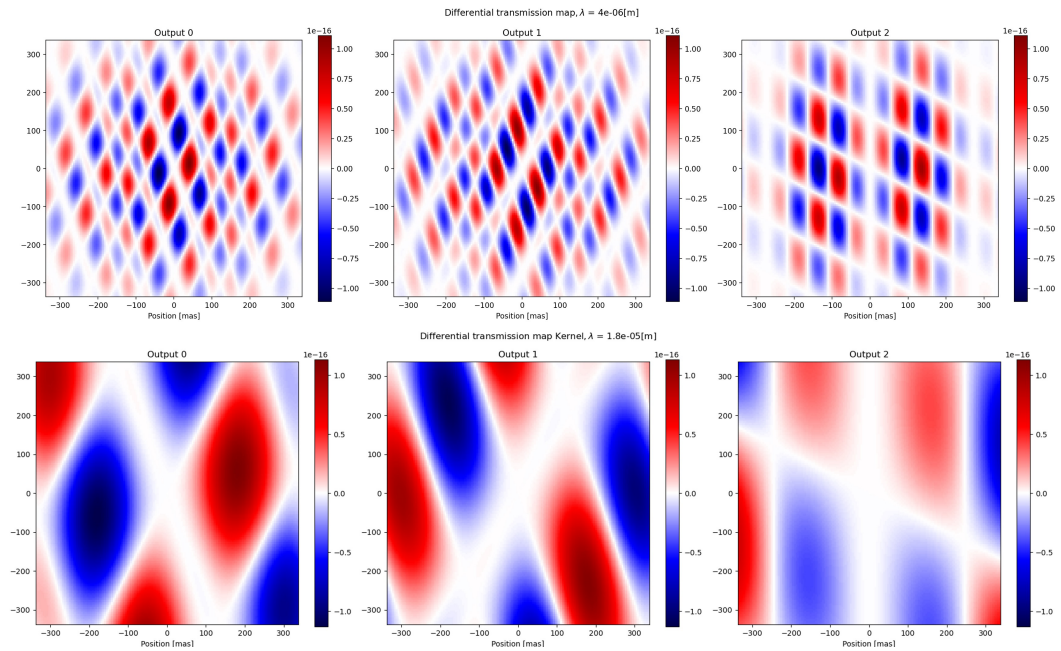


Figure A.10: Differential transmission maps for the kernel configuration showing the recombination of the six dark outputs. The displayed maps show the differential output at $4 \mu\text{m}$ and $18 \mu\text{m}$.

Modulations and efficiencies

The three differential map consequently also lead to three modulation signals, shown in Figure A.11. For the efficiencies in Figure A.12 the contributions from these three signals are summed to display the total modulation efficiency of the instrument.

Figure A.11: Signal modulations across the spectral regime for the kernel configuration, following from the differential transmission map for a planet at $[0, 100]$.

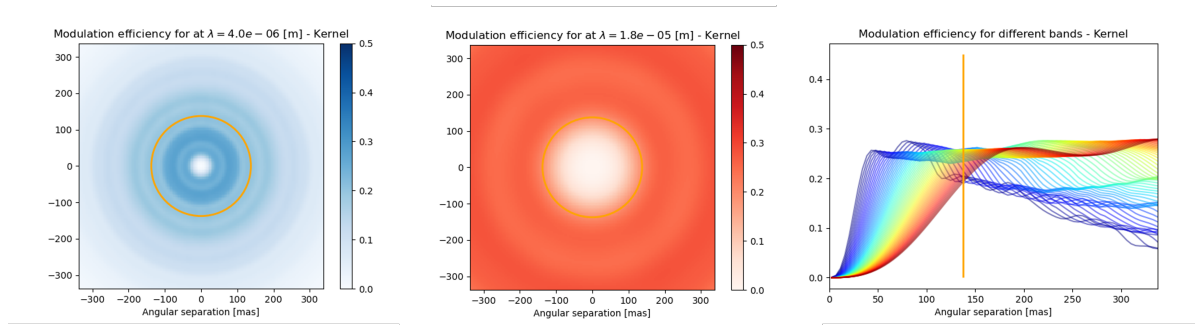


Figure A.12: Modulation efficiencies for the rectangular configuration. The left two plots show the modulation efficiencies for spectral channel $4 \mu\text{m}$ and $18 \mu\text{m}$ in the observed field. the righter most plot shows the development of the modulation efficiencies as a function of separation for all wavelengths. The orange indicator shows the $\frac{\lambda}{B}$ separation at $10 \mu\text{m}$

A.2. Additional results

Below follow some supporting graphs that were produced over the course of the research.

A.2.1. Single planet

In the results section a corner plot showing the MCMC fitting results was displayed, in Figure A.13 the same corner plot is displayed in larger format for easier readability.

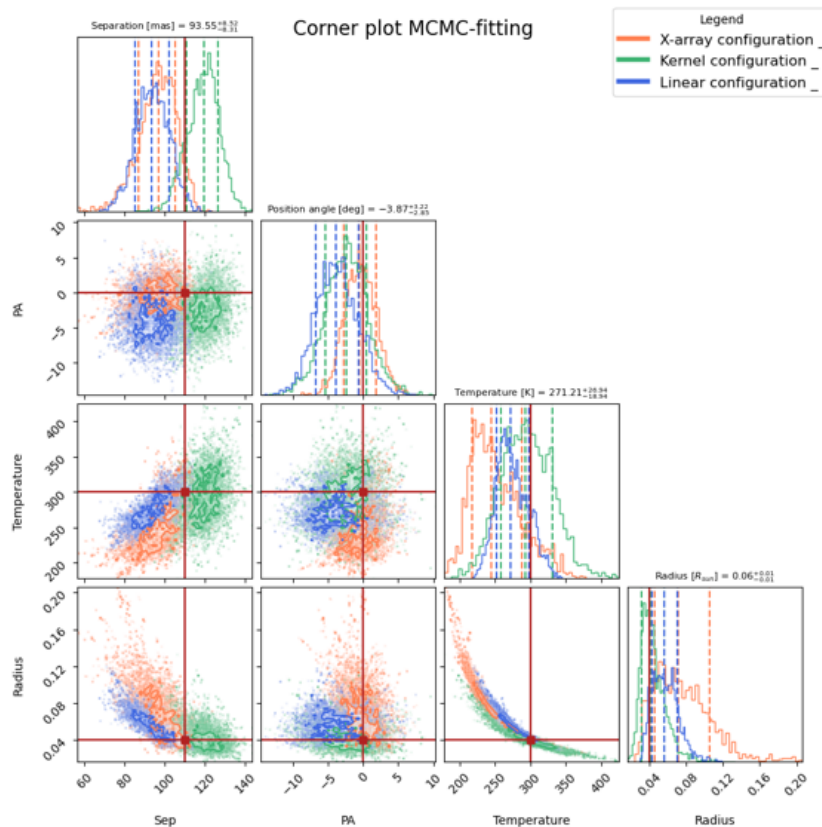


Figure A.13: MCMC corner plot result in a larger format. Simulated planet has properties: $R = 4.4 R_e$, $T = 300 \text{ K}$, $\text{Sep} = 110 \text{ mas}$, $\text{PA} = 0$.

Previously the resulting fitting of a single planet with varying planet radii was shown. To verify if the results hold true the experiment was repeated for varying planet separations and planet temperatures. The results are shown in respectively Figure A.14 and Figure A.15. The temperature results are for a

single fitting only instead of a full MCMC simulation due to limited server capacity. It can be observed that again the configurations perform very similarly.

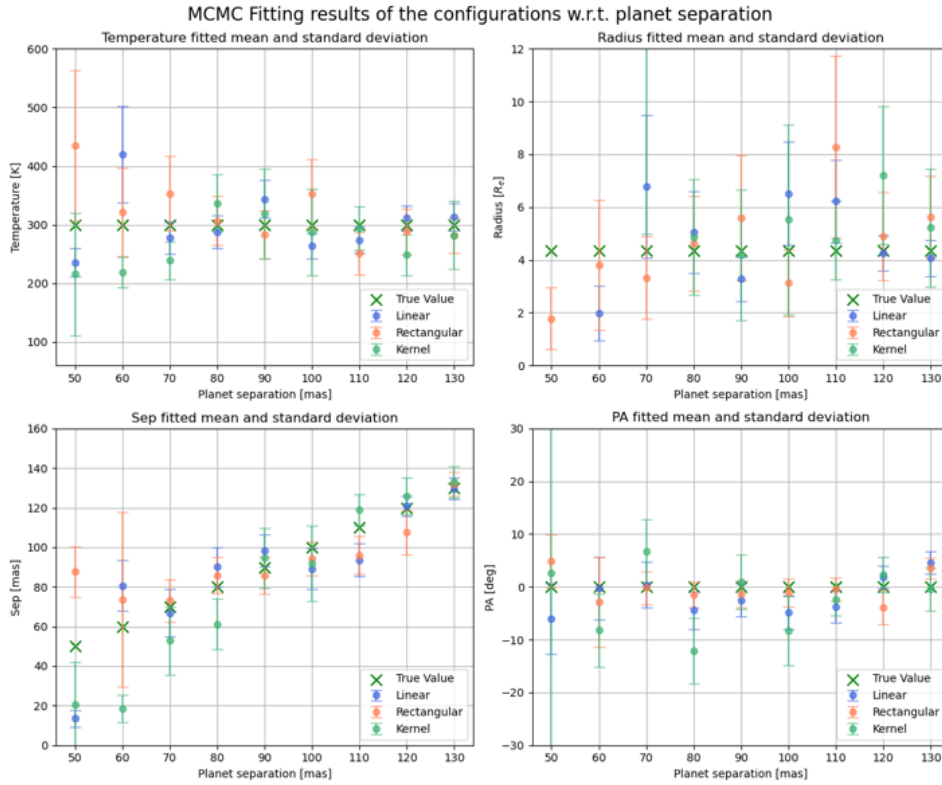


Figure A.14: MCMC fitting results with a varying planet separation. The planet parameters used are $T = 300$ K, $R = 4.4 R_e$, $PA = 0$ deg

In the presented results the fitting results were shown with a zoom, to show the original full results a non-zoomed version is presented in Figure A.16.

A.2.2. Correlations

In literature the separation $\frac{\lambda}{2B}$ is sometimes used as inner working angle, this separation indicates the first constructive fringe that is formed in the interference. The same correlation plot is displayed in Figure A.17 which indicates this separation instead.

A.2.3. Two planets

The two planet fitting was repeated for a case where the planets were separated by 100 mas (1 AU), the fitting result is presented in Figure A.18.

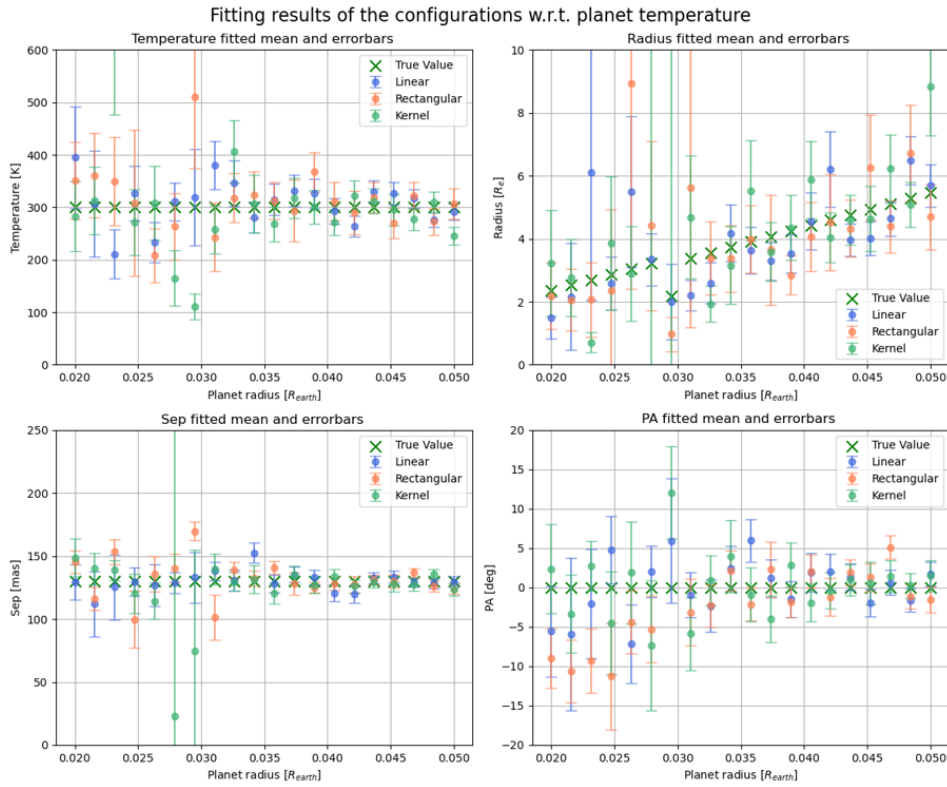


Figure A.15: Single fitting results for a single planet with a varying planet temperature. The planet parameters used are sep = 130 mas, R = 4.4 R_e , PA = 0 deg

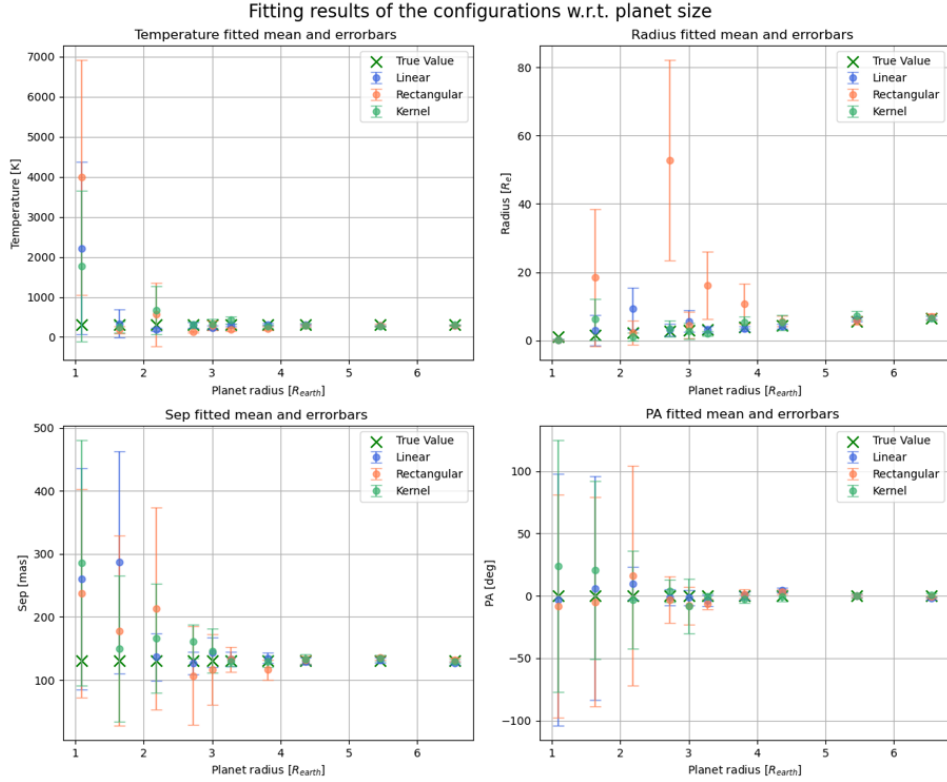


Figure A.16: Single planet fitting w.r.t. radius without zoom

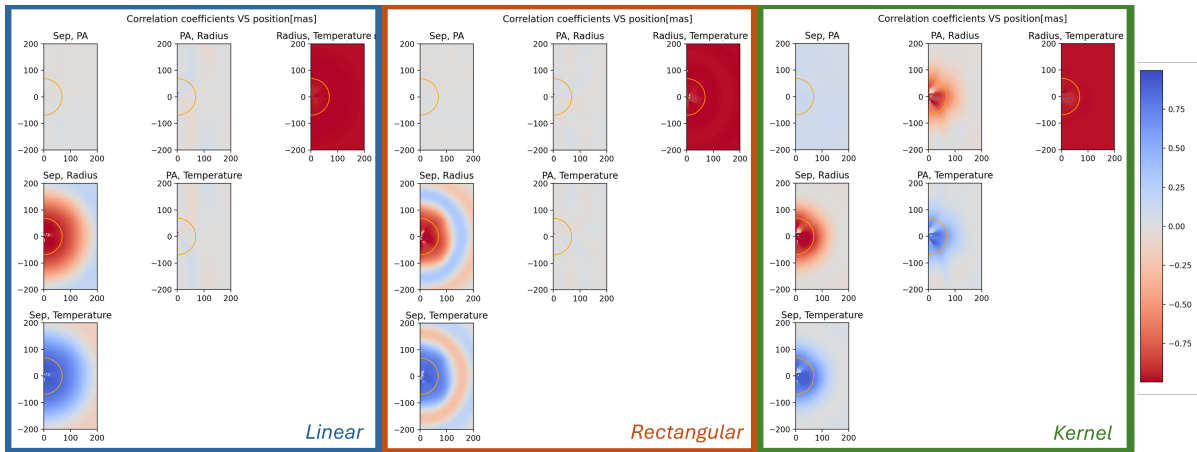


Figure A.17: Maps of the correlation levels between each parameter pair with indication of $\frac{\lambda}{2B}$. A blue color indicates a positive correlation between the parameters and red a negative correlation.

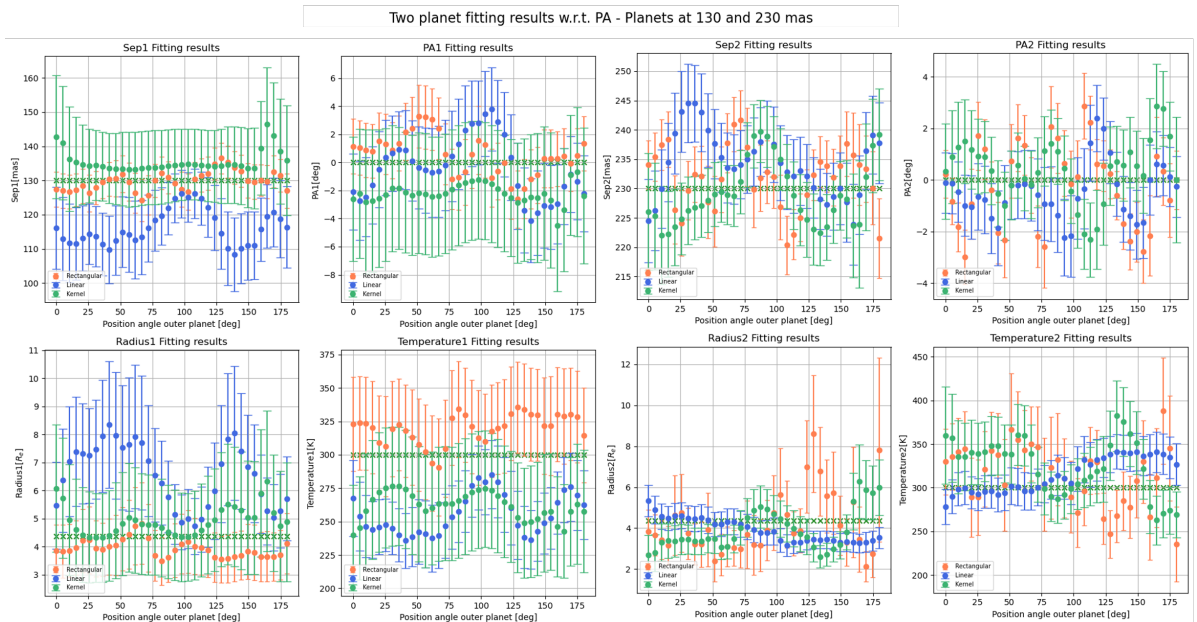


Figure A.18: Results of a two planet fitting with two planets with size $R = 4.4 R_E$, $T = 300$ K. The planets are located at 130 mas (planet 1) left four plots and at 230 mas (planet 2) shown in the right plots.